

See discussions, stats, and author profiles for this publication at: <https://www.researchgate.net/publication/276148197>

Experimental (X-ray, ^{13}C CP/MAS NMR, IR, RS, INS, THz) and solid-state DFT study on (1:1) Co-crystal of bromanilic acid and 2,6-dimethylpyrazine

ARTICLE in THE JOURNAL OF PHYSICAL CHEMISTRY B · MAY 2015

Impact Factor: 3.3 · DOI: 10.1021/acs.jpcc.5b03279 · Source: PubMed

READS

79

4 AUTHORS, INCLUDING:



Katarzyna Luczynska

Joint Institute for Nuclear Research

5 PUBLICATIONS 3 CITATIONS

SEE PROFILE



Krzysztof Lyczko

Institute of Nuclear Chemistry and Technolog...

23 PUBLICATIONS 88 CITATIONS

SEE PROFILE



Jan Dobrowolski

AGH University of Science and Technology in ...

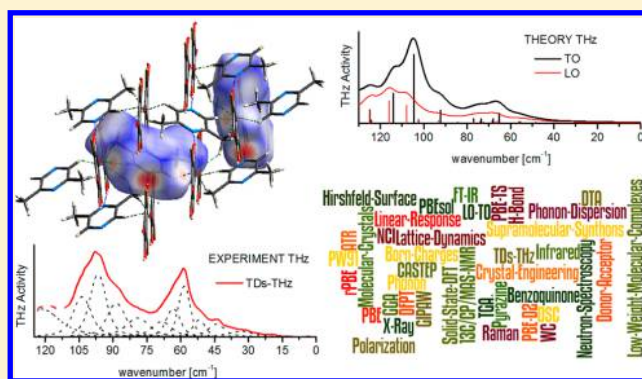
34 PUBLICATIONS 93 CITATIONS

SEE PROFILE

Experimental (X-ray, ^{13}C CP/MAS NMR, IR, RS, INS, THz) and Solid-State DFT Study on (1:1) Co-Crystal of Bromanilic Acid and 2,6-DimethylpyrazineKatarzyna Łuczyńska,^{*,†,‡} Kacper Drużbicki,^{‡,§} Krzysztof Lyczko,[†] and Jan Cz. Dobrowolski^{†,||}[†]Institute of Nuclear Chemistry and Technology, 16 Dorodna Street, 03-195, Warsaw, Poland[‡]Frank Laboratory of Neutron Physics, Joint Institute for Nuclear Research, 141980, Dubna, Russian Federation[§]Department of Radiospectroscopy, Faculty of Physics, Adam Mickiewicz University, Umultowska 85, 61-614, Poznan, Poland^{||}National Medicines Institute, 30/34 Chelmska Street, 00-725 Warsaw, Poland

S Supporting Information

ABSTRACT: A combined structural, vibrational spectroscopy, and solid-state DFT study of the hydrogen-bonded complex of bromanilic acid with 2,6-dimethylpyrazine is reported. The crystallographic structure was determined by means of low-temperature single-crystal X-ray diffraction, which reveals the molecular units in their native protonation states, forming one-dimensional infinite nets of moderate-strength $\text{O}\cdots\text{H}\cdots\text{N}$ hydrogen bonds. The nature of the crystallographic forces, stabilizing the studied structure, has been drawn by employing the noncovalent interactions analysis. It was found that, in addition to the hydrogen bonding, the intermolecular forces are dominated by stacking interactions and $\text{C}\cdots\text{H}\cdots\text{O}$ contacts. The thermal and calorimetric analysis was employed to probe stability of the crystal phase. The structural analysis was further supported by a computationally assisted ^{13}C CP/MAS NMR study, providing a complete assignment of the recorded resonances. The vibrational dynamics was explored by combining the optical (IR, Raman, TDs-THz) and inelastic neutron scattering (INS) spectroscopy techniques with the *state-of-the-art* solid-state density functional theory (DFT) computations. Despite the quasi-harmonic approximation assumed throughout the study, an excellent agreement between the theoretical and experimental data was achieved over the entire spectral range, allowing for a deep and possibly thorough understanding of the vibrational characteristics of the system. Particularly, the significant influence of the long-range dipole coupling on the IR spectrum has been revealed. On the basis of a wealth of information gathered, the recent implementation of a dispersion-corrected linear-response scheme has been extensively examined.



I. INTRODUCTION

In recent years, hydrogen-bonded, donor–acceptor type supramolecular co-crystals have attracted much interest for their potential use as functional materials, as the compounds may show multiple intriguing and not yet completely understood properties. The donor–acceptor nature of the quoted systems often has a dual meaning, being related both to the electron- and proton-transfer phenomena, which can give rise to the semiconducting or ferroelectric properties.

Among an increasing number of reported systems, a particular interest has been given to the complexes of anilic acids, which can act both as proton donors and as electron acceptors.^{1–3} For example, much attention has been already paid to the semiconducting properties of pure and functionalized (electron donating) tetrathiafulvalene (TTF) complexes with (electron accepting) chloranilic acid (CIA), where the mixed stacks of both counterparts give rise to the one-dimensional conductivity.^{4,5} In addition, great attention has been paid to the proton donating

properties of anilic acids, which—along with the molecular displacive tendency—can finally lead to the ferroelectricity in molecular solids. The prime examples, originally presented by Horiuchi et al., are the phenazine complexes of anilic acids.^{6–8}

Furthermore, one may expect that the interest in use of organic acid complexes, particularly that of benzoquinones, may even increase in the future. For example, in the search of low-polluting electrode materials for batteries, the use of redox-active organic compounds represents a promising alternative to the conventional metal-based systems. Recently, Bonnard et al. have shown that *p*-benzoquinone derivatives may be a promising candidate for lithium insertion.⁹

In addition to its broad and barely uncovered potential for practical utility, the donor–acceptor hydrogen bond complexes

Received: April 6, 2015

Revised: May 9, 2015

Published: May 11, 2015



are also cognitively intriguing. Small, molecular hydrogen-bonded synthons are crucial for supramolecular chemistry and crystal engineering,¹⁰ especially for designing multicomponent crystals.¹¹ In such a case, the specific, competing intermolecular interactions are the most important factor. Thus, the progressive exploration of the low-weight molecular complexes in the interactions–structure interplay becomes an important issue, for which crystallography, nuclear magnetic resonance, as well as vibrational spectroscopy play a central role.¹² The anilic acid complexes with organic bases are, therefore, good examples of the systems, where one can expect the presence of most known specific interactions—including hydrogen or halogen bonding.

Nevertheless, even a perfect experiment can lead to an ambiguous interpretation. This is why the full understanding of such relations requires employing of the theoretical calculations. At the limit of the current computational resources, density functional theory (DFT) remains the most powerful tool giving the results of reasonable accuracy. Despite its systematic deficiencies, it can be successfully applied in calculations of periodic systems, and thereby used to elucidate the structure–spectroscopy response relation.

In the present paper, we report an extensive, joint structural and spectroscopic study of a polar, one-dimensional, low-weight hydrogen bonded molecular complex, representing the family of the anilic acid:pyrazine-type base conjugates. The low-temperature crystal structure is reported along with the complementary vibrational spectroscopy analysis, which was fully supported by the *state-of-the-art* static-DFT computations, shedding light on the molecular internal modes and the lattice dynamics. By combining several experimental techniques with the theory, we were able to examine the performance of modern solid-state calculations in description of the vibrational spectra of a middle-strength hydrogen-bonded molecular complex and—what is more—find a ternary structure–intermolecular interaction–spectrum relationship.

The analysis of the external factors driving the vibrational spectra of polar molecular assemblies requires a possibly accurate theoretical methodology. Hence, the performance of the semilocal DFT has been tested at the limits of its accuracy. Thanks to the recent implementation of the dispersion-corrected linear-response methodology, the performance of the semi-empirical van der Waals (vdW) corrections has been critically examined with an emphasis on the vibrational spectroscopy as referring both to the internal and intermolecular vibrations.

Due to the wealth of information gathered, each part of the paper—discussing the results in detail—has been prefixed by the research outline and shortly summarized as to highlight the most important findings.

II. EXPERIMENTAL AND COMPUTATIONAL DETAILS

Sample Preparation. Bromanilic acid (2,5-dibromo-3,6-dihydroxy-*p*-quinone; BrA; $C_6H_2Br_2O_4$) and 2,6-dimethylpyrazine (2,6-DMP; $C_6H_8N_2$) were used as purchased (purity >98.0%) from TCI EUROPE N.V. The equimolar amounts of both compounds were dissolved in methanol and magnetically stirred at 30 °C. The co-crystals of BrA:2,6-DMP (2,5-dibromo-3,6-dihydroxycyclohexa-2,5-diene-1,4-dione 2,6-dimethylpyrazine) were grown by slow evaporation from a dark orange liquid under ambient conditions. The entire process took place over a period of less than 2 weeks.

Thermal Analysis. The thermal stability of the sample (13.6 mg) was examined in an argon atmosphere at a heating rate of 5 °C/min, using a TA SDT Q600 thermogravimetric analyzer. The

calorimetric analysis was performed with a TA DSC Q2000 calorimeter, varying the temperature from −170 °C up to the decomposition point. Since one could expect the presence of a weak second-order-type phase transition, the heating/cooling rate of 20 °C/min was used along with a large sample mass (34.9 mg).

Single-Crystal X-ray Diffraction. Diffraction measurements were done at 100 K (−173.15 °C) with an Agilent Technologies SuperNova (Dual Source) single-crystal diffractometer, equipped with an EOS CCD detector and mirror-monochromated Cu $K\alpha$ radiation ($\lambda = 1.54184$ Å) from a microfocused Nova X-ray source. Data collection (ω -scans) and processing were performed with the CrysAlis Pro program package. The structure was solved by direct methods and refined by the full-matrix least-squares method on F^2 data using SHELXTL programs.¹³ All non-hydrogen atoms were refined anisotropically. The H atoms bonded to the C atoms were placed in calculated positions with C–H = 0.98 (methyl) or 0.95 Å (aromatic) and refined isotropically using a riding model with $U_{iso}(H)$ equal to $1.5U_{eq}(C)$ or $1.2U_{eq}(C)$ for methyl and aromatic H atoms, respectively. In turn, the H atoms of the OH groups were located in a difference map and their positions were freely refined with $U_{iso}(H)$ set to $1.5U_{eq}(O)$. Crystal graphics were generated by the VESTA program.¹⁴ The crystallographic data and structural refinement parameters are summarized in Table 1.

The crystallographic data for this paper are deposited at the Cambridge Crystallographic Data Center (CCDC 1023741).

Table 1. Crystallographic Data and Structure Refinement Parameters for BrA:2,6-DMP (1:1)

molecular formula	$C_{12}H_{10}Br_2N_2O_4$
formula weight	406.04
temperature (K)	100 (2)
λ [CuK α] (Å)	0.71073
crystal system	monoclinic
space group	$P2_1/c$
unit cell dimensions	
<i>a</i> (Å)	11.7288 (5)
<i>b</i> (Å)	14.1905 (5)
<i>c</i> (Å)	8.5037 (3)
α (deg)	90.00
β (deg)	105.162 (4)
γ (deg)	90.00
volume (Å ³)	1366.07 (9)
<i>Z</i>	4
<i>D_c</i> (g cm ^{−3})	1.974
μ (mm ^{−1})	5.948
<i>F</i> (000)	792
crystal size (mm)	0.25 × 0.18 × 0.12
Θ range for data collection (deg)	3.02–31.10
reflections collected	8515
independent reflections	3988
<i>R_{int}</i>	0.0414
absorption correction	multiscan
transmission, <i>T_{min}</i> / <i>T_{max}</i>	0.43649/1.0000
data/restraints/parameters	3988/0/189
goodness of fit on F^2	1.064
final <i>R</i> indices [<i>I</i> > 2 σ (<i>I</i>)]	<i>R</i> 1 = 0.0375; <i>wR</i> 2 = 0.0797
<i>R</i> indices (all data)	<i>R</i> 1 = 0.0481; <i>wR</i> 2 = 0.0856
largest diff. peak/hole (e Å ^{−3})	0.868/−1.141

These data can be obtained free of charge via www.ccdc.cam.ac.uk/data_request/cif.

Solid-State Nuclear Magnetic Resonance (^{13}C CP/MAS NMR). A ^{13}C cross-polarization magic angle spinning (CP/MAS) NMR spectrum was acquired at room temperature, using a Bruker Avance III spectrometer (16.5 T), operating at the ^1H Larmor frequency of 700.27 MHz and the ^{13}C Larmor frequency of 176.08 MHz. The powder sample was placed in a 3 mm diameter zirconia rotor and spun at a frequency of 18 kHz. 640 scans were then accumulated with a cross-polarization contact time of 2.5 μs and a recycle delay of 6 s. The ^{13}C chemical shifts were referenced with respect to tetramethylsilane (TMS).

Optical Vibrational Spectroscopy (FT-IR, FT-RS, TDs-THz). The optical vibrational spectroscopy measurements were performed at room temperature, using powder samples. All the infrared measurements were made at a spectral resolution of 2 cm^{-1} , by accumulating 64 scans. The middle-FT-IR spectroscopy was applied in both absorption and attenuated total reflectance (ATR) modes. The transmission spectrum was recorded for a KBr pellet, with a Bruker Equinox 55 FT-IR spectrometer, equipped with a deuterated triglycine sulfate (DTGS) detector and a silicon carbide (Globar) source. The ATR measurements were performed with a Nicolet iS10 FT-IR spectrometer, using a diamond crystal, Globar source, and a DTGS detector. Both spectra were recorded in the range of 4000–400 cm^{-1} . The far-infrared absorption measurements were carried out with a Bruker Vertex v70 vacuum spectrometer, equipped with a polyethylene detector and Globar source. The sample was suspended in Apiezon N grease and placed on a polyethylene disc.

The FT-Raman spectroscopy measurements were performed over the range of 4000–50 cm^{-1} , using a Bruker Raman FRA 106/S module, equipped with a germanium detector and the 1064 nm excitation line of a Nd:YAG laser. The spectral resolution of 2 cm^{-1} and accumulation of 2000 scans were chosen as the experimental conditions.

The time-domain terahertz (TDs-THz) spectroscopy study was performed in the transmission mode, using a Teraview TPS 3000 unit. The sample was ground using a mortar and pestle in order to reduce the particle size and avoid the scattering loss. A mixture containing 10% of the sample and 90% of high-density polyethylene (HDPE) was prepared to obtain a 400 mg pellet. A pure polyethylene sample was used as a reference. The spectrum was acquired by accumulation of 1800 scans.

Inelastic Neutron Scattering (INS) Spectroscopy. The INS measurements were performed with the inverted geometry spectrometer NERA,¹⁵ set at the high flux pulsed nuclear reactor IBR-2 at JINR Dubna, Russian Federation. The incident neutron energies were determined by measuring the neutron time-of-flight across the 110 m distance from the IBR-2 water moderator to the sample. The INS spectra were recorded simultaneously for all the wavelengths/energies across the scattering angles varying from 20 to 160°. The INS spectrum was collected at the final energy of the scattered neutrons equal to $E_f = 4.65$ meV, which was fixed by the crystal analyzers and beryllium filters. The ~ 10 g sample was measured for 17 h at a temperature of 10 K.

Computational Details. Density functional theory (DFT) calculations in periodic boundary conditions (PBC) were performed with the plane-wave/pseudopotential method implemented in Cambridge Serial Total Energy Package (CASTEP) v. 6.1 and v. 8.0.^{16,17} Exchange and correlation were defined using a standard Perdew–Burke–Ernzerhoff (PBE) generalized gradient approximation (GGA),^{18,19} as well as with the so-called “hard”²⁰ PBE revision proposed by Hammer

(rPBE).²¹ In addition, several available approximations were used to probe the functional influence on the crystal-cell description, including the original PW91^{22,23} and “soft”²⁰ GGA functionals, namely, the one proposed by Wu and Cohen (WC)²⁴ and the PBEsol revision.²⁵ Moreover, the dispersion-corrected PBE has been extensively examined by employing semiempirical corrections in the original Grimme’s D2 scheme²⁶ as well as by using the Tkatchenko and Scheffler approach.²⁷

Hard, norm-conserving pseudopotentials (NCPPs), constructed according to the Rappe–Rabe–Kaxiras–Joannopoulos (RRKJ)^{28,29} scheme, were used at the 1050 eV plane-wave kinetic energy cutoff. In order to ensure a highly reliable convergence of the low-energy phonon range, the baseline size was multiplied by a factor of 4, as referring to the kinetic energy cutoff for the charge density and potential. The Monkhorst–Pack grid was kept to maintain a k -spacing of 0.07 \AA^{-1} . The quoted settings allow one to achieve the convergence in variation of the total energy, maximum force, external stress, maximum displacement, and SCF iterations better than 1×10^{-10} eV/atom, 1×10^{-5} eV/ \AA , 1×10^{-3} GPa, 1×10^{-6} \AA , and 1×10^{-12} eV/atom, respectively.

The phonon frequencies were obtained by diagonalization of the dynamical matrices computed using density functional perturbation theory (DFPT; linear response).^{17,30–35} Thanks to the recent implementation of the dispersion corrections in the linear-response methodology, the vibrational analysis was performed following both the fixed cell and full optimization of the crystal structure. For the frequencies computed at the zero-wavevector, the acoustic sum rule (ASR) was imposed.

The Raman activity tensors were calculated using a hybrid finite displacement/DFPT method in the presence of an external field³⁶ and finally transformed into the Raman intensities, by taking into account the excitation line and the thermodynamic conditions.³⁷

The influence of the LO–TO splitting on the IR spectrum was probed by using the computed permittivity and Born charge tensors. The nonanalytic contribution, generating the long-range dipole coupling, was added in the most polar direction approaching the Γ point.

In addition to the direct evaluation of the frequencies and intensities at the Γ point, the phonon dispersion relations were calculated along the high symmetry paths throughout the Brillouin zone. For this purpose, the dynamical matrices were computed on a regular grid of wavevectors and Fourier interpolation was used to extend the computed grid to a desired fine set of points along the high-symmetry directions.³⁸ From the computed eigenfrequencies and eigenvectors, the inelastic neutron scattering intensities were predicted with the help of the aClimax program.³⁹

The ^{13}C NMR calculations were performed with the gauge-including projector-augmented wave (GIPAW) method,⁴⁰ implemented in the CASTEP NMR module. The all-electron information, needed for calculation of the absolute NMR chemical shielding tensors, was reconstructed for the above quoted NCPP equilibrium geometries, using *on-the-fly* generated scalar relativistic ultrasoft pseudopotentials (USPPs),⁴¹ by using the same numerical settings as quoted above.

III. RESULTS

Thermal Stability. Thermal stability of a native crystal structure along with possible polymorphism has a primary meaning. In the case of donor–acceptor molecular complexes, the volatile nature of the hydrogen-bonded components often

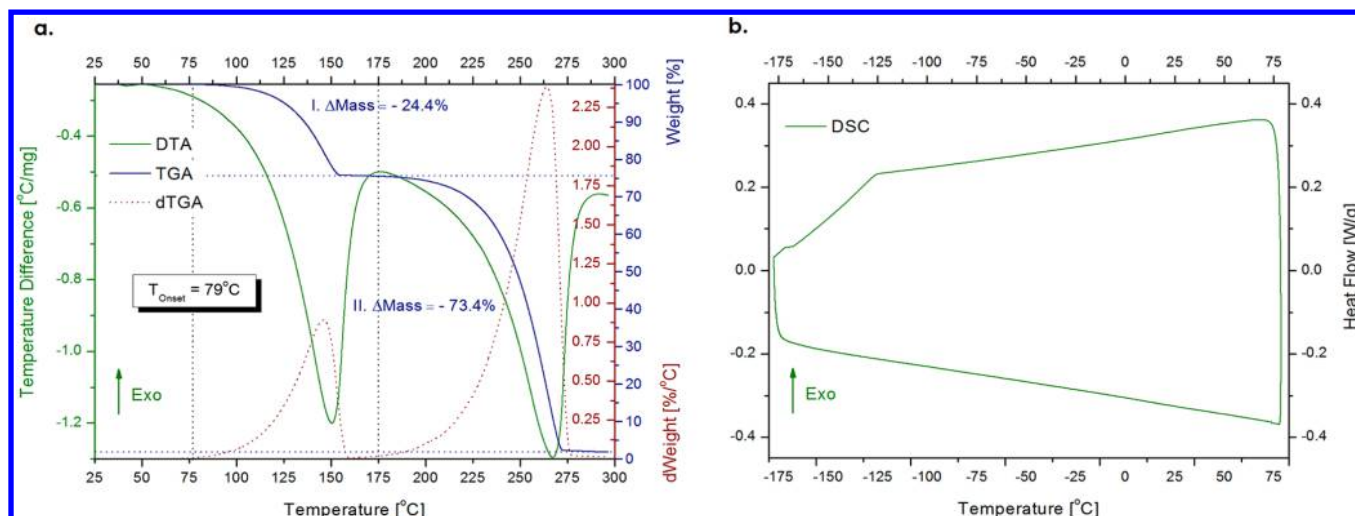


Figure 1. (a) Thermogravimetric (TGA; dTGA) and differential thermal analysis (DTA) of BrA:2,6-DMP (1:1) co-crystal in the temperature range 25–300 °C. (b) Differential scanning calorimetry (DSC) curve for the title compound, recorded in the range from -175 to 80 °C. Note that the break of the baseline on the DSC curve is an apparatus effect due to a high-speed cooling requested.

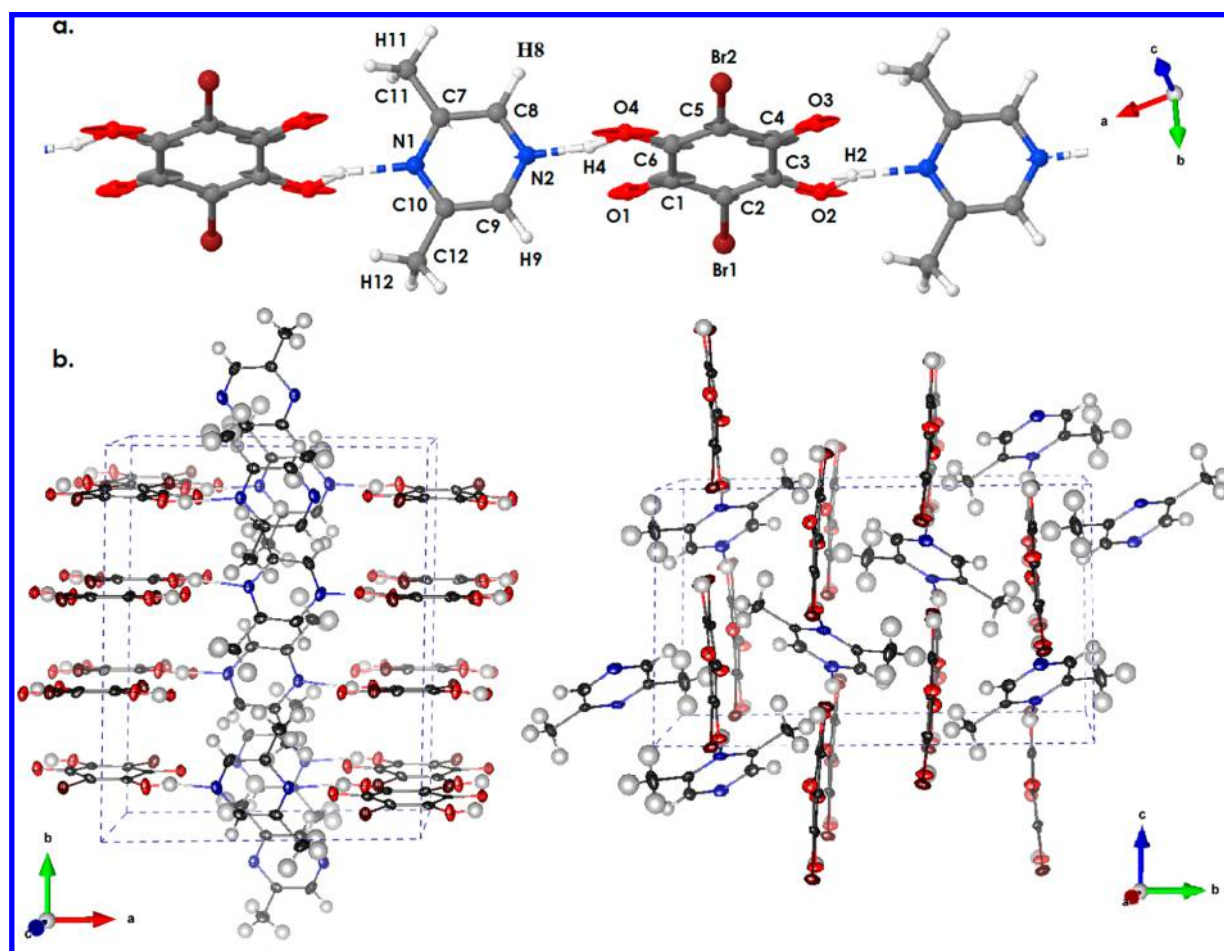


Figure 2. Crystal structure of BrA:2,6-DMP (1:1) co-crystal measured at 100 K. The hydrogen-bonded units are given in part a along with the adopted atomic labeling. The Born charge tensors are presented as ellipsoids (calculated at the PBE-NCPP-1050 eV theory level). The crystal packing is presented in the unit cell projection toward the *c*- and *a*-axes (b), with the thermal ellipsoids of 80% probability given.

makes the compounds relatively unstable, while possible phase transitions are often expected to be extremely subtle. The polymorphism is then most often related to the subtle, molecular displacement structural transformations, usually expected to be observed at lower temperatures, or with higher-temperature

order–disorder transitions, which can be generally associated with proton migration.

Figure 1 presents the results of the thermogravimetric (a) and calorimetric (b) analysis of the studied material. The thermogravimetry reveals a well-resolved two-step decomposi-

Table 2. Cell Parameters and Volume of the BrA:2,6-DMP (1:1) Unit Cell as Found with Single-Crystal X-ray Diffraction at 100 K along with the Periodic DFT Calculations (at 0 K)

method	BrA:2,6-DMP (1:1) unit cell						
	<i>a</i> (Å)	<i>b</i> (Å)	<i>c</i> (Å)	α (deg)	β (deg)	γ (deg)	<i>V</i> (Å ³)
X-ray 100 K	11.7288(5)	14.1905(5)	8.5037(3)	90.00	105.162(4)	90.00	1366.07(9)
PBE-D2	11.4016	14.31420	8.5940		105.27		1353.05
PBE-TS	11.5046	14.4931	8.6557		105.35		1391.77
PBEsol	11.4306	15.9652	8.7286		107.38		1520.21
PBE	11.6756	17.1851	9.2191		108.51		1754.05
WC	10.8944	18.2310	10.3048		110.82		1913.00
PW91	11.0182	18.3388	10.1957		109.38		1943.48
rPBE	11.8644	19.0445	9.9906		109.62		2126.37

tion of the sample. The compound was found to be stable up to 79 °C. In the first step, the 24.4% mass loss was observed, which matches well the stoichiometric mass content of 2,6-DMP (26.8%). Starting from 175 °C, the remaining BrA is emitted which corresponds to the 73.4% loss of mass (73.2% is expected). The decomposition is associated with a purely endothermic nature of the DTA curve in the entire temperature range, suggesting a simple decomposition mechanism.

The high-quality calorimetric analysis clearly shows that no phase transitions occur down to −175 °C. As mentioned, one can expect very weak second-order or specific-heat discontinuity transitions, which could undergo blurring with slow temperature changes. For that reason, the DSC measurements were performed with a high-speed ramp (20 °C/min) and a large mass (34.9 mg) of the sample.

Therefore, the high stability of the native phase is confirmed down to −175 °C. In addition, the theoretical vibrational analysis discussed below did not reveal any mechanical instabilities of the phonon modes, which would suggest the presence of a very-low temperature structure with lowered symmetry.

Crystal and Molecular Structure. The primary question on the studied material is the crystallographic structure, which gives the reference for further considerations and reflects the specific intermolecular interactions stabilizing the co-crystal. In order to understand the structural properties, the low-temperature (100 K), single-crystal X-ray diffraction has been employed. In addition to the experimental study, the performance of the semilocal, periodic DFT calculations has been examined as referring to its potential ability for accurate description of both the cell parameters and the internal coordinates.

The molecular structure of the title system, containing bromoanilic acid and 2,6-dimethylpyrazine in a 1:1 molar ratio, is presented in Figure 2. In principle, it can be described as a supramolecular superstructure built by the hydrogen-bonded ...2,6-DMP...BrA... chains, which are formed by alternating molecules, propagated toward the crystallographic axis *a* (see Figure 2a). According to the X-ray study, the neighboring acid and base molecules are linked into chains by a pair of nonequivalent intermolecular hydrogen bonds. The alternating molecular planes of BrA and 2,6-DMP are twisted to each other by about 66.1(2) (C4–C3–N1–C7 torsion angle) or 68.6(2)° (C1–C6–N2–C9 torsion angle). The final selection of the theoretical calculations, discussed in more detail later on, provides values of ~62.3–66.7°. For the superposition of the experimental and theoretical structures, we refer the reader to the Supporting Information.

The system crystallizes in the monoclinic, centrosymmetric *P*₂/c (*C*_{2h}⁵) space group, with four molecular formulas equivalent by symmetry per unit cell (see Figure 2b). The

asymmetric part contains the single molecules of both counterparts. The molecular chains in the crystal are arranged in opposite directions (an anticlinic configuration), where the associated polarization vectors compensate each other, resulting in the centrosymmetric structure, and prevent the appearance of spontaneous polarization in the system.

By analyzing the crystal structure, one can therefore try to understand the phase stability. According to the crystallographic data and subsequent theoretical calculations, there is no proton transfer between the molecules, since both moieties occur in their inert protonation states. Such an assumption stays in line with the data reported for the isostructural, chloranilic acid analogue by Asaji and co-workers.⁴² In the quoted paper, the spin–lattice ³⁵Cl NQR relaxation time measurements were performed across a wide temperature range, where it was concluded that the relaxation is dominated by lattice vibrations, suggesting no transfer motion of proton between the acid and base molecules.

We have then optimized the crystal phase without any symmetry constraints (standard, fixed-cell PBE calculations), with an alternative, hypothetical synclinc chain orientation. The structural optimization leads to the proton migration toward nitrogen in half of the molecules, while, however, the second ones are sterically restrained. The hypothetical phase was found to be higher in total energy by 89 kJ/mol per cell. Due to the steric hindrance induced by the methyl groups, transition into such a synclinc state is highly undesirable, as it would require the reorientation of the whole 2,6-DMP units in the *ab* plane. Such an analysis claims a high stability of the studied phase and stays in line with Asaji's ³⁵Cl NQR results.⁴² Such information is relevant from the point of view of crystal engineering, as it might suggest that the 2,6-DMP...BrA configuration tends to be very stable.

In order to look deeper into the crystal structure, the theoretical calculations in periodic boundary conditions were employed, which however deserve a comment. A well-known deficiency of density functional theory (DFT) is associated with the van der Waals (vdW) forces description, which are generally related to the long-range electron correlation effects, being notoriously absent from the local and semilocal density functionals. Such a shortcoming explains the failure asymptotic behavior of the interaction energy between nonpolar systems and results in a significant deviation in predicted cell constants. In general, two practical strategies have been applied to treat the dispersion forces. The first one is the reparameterization of existing functionals, for example, according to Truhlar et al.^{43–45} or construction of novel nonempirical functionals such as vdW-DF.^{46–49} An alternative way is an *ad hoc* approach, which includes an empirical correction term associated with the vdW forces description separate from a DFT functional. Most

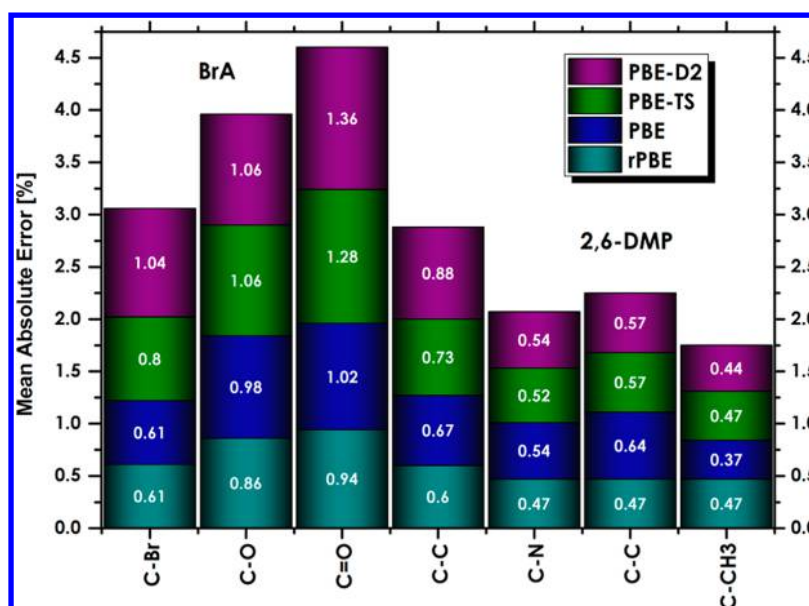


Figure 3. Mean absolute errors (%) between selected bonds in BrA:2,6-DMP (1:1) co-crystal as delivered by theoretical calculations with respect to the experimental X-ray data at 100 K. The rPBE and PBE data refers to the constrained-cell relaxation, while the PBE-TS and PBE-D2 results correspond to the full optimization.

commonly, the dispersion correction of the form $E_{\text{disp}} = -s_6 \sum_i \sum_j \sum_g (C_6^{ij}/R_{ij,g}^6) f_{\text{dmp}}(R_{ij,g})$ is added to the DFT total energy for each pair (ij) of atoms, separated by a distance of R_{ij}^{-6} , where the energy correction is then summed over all atom pairs and g lattice vectors.⁵⁰ The function $f(R_{ij})$ is a damping function, which is necessary to avoid a divergence for small values of R , while C_6^{ij} is the dispersion coefficient for a pair of atoms and s_6 is a global scaling factor. Each *ad hoc* scheme uses slightly different damping functions and coefficients. Here, the Grimme's corrections (D2) were applied, where the C_6^{ij} coefficients depend only on the chemical species. In contrary, in the Tkatchenko–Scheffler methodology, the coefficients are calculated *on-the-fly* by scaling the free-atom values using Hirshfeld atomic volumes, therefore factoring in the effect of the chemical environment.

Recently, we have examined the performance of several available DFT functionals along with the vdW corrections by referring to the normal-pressure polymorphs of resorcinol.⁵¹ Here, we would like to further extend the analysis into the influence of the vdW corrections on the vibrational properties of the studied system.

The cell parameters of the title system are collected in Table 2 and juxtaposed with the results of solid-state DFT calculations. By analyzing the table, one can clearly note the failure of pure DFT in description of the cell parameters. While the dominating, electrostatic contribution in the hydrogen bond can be properly reproduced as referring to the a -constants, it utterly fails in description of both b - and c -lengths, which are mainly driven by the vdW forces. The optimization under atmospheric pressure results in the striking errors, varying from ~ 11 (PBEsol) to 56% (rPBE) with respect to the experimentally determined cell volume. In line with our previous reports,⁵¹ the ability of semilocal DFT to describe the cell parameters supports an expected hierarchy: GGA-TS > GGA-D2 > “soft” > “standard” > “hard” GGA. While both “soft” GGA, namely, PBEsol and WC, are expected to act similarly, there is however no advantage of using WC with respect to standard PBE. Similarly, one can observe a slightly different performance of PBE and PW91, which are conceptually recognized as nearly equivalent. As expected,⁵¹

the worst description of the cell parameters was found with “hard” rPBE.

While PBE-TS is generally recognized as a more accurate approach than PBE-D2, we observe their similar performance here, where the volume has been described even slightly better with the original Grimme's scheme as reducing the volume error down to -1% ($+1.9\%$ with PBE-TS). In addition, since we have already shown that “soft” GGA does not provide any advantage in the calculations of the internal coordinates and vibrational spectra of molecular solids, we are limiting our further analysis to the “hard” and “standard” GGA along with the most promising vdW corrections available in the present linear-response implementation.

Most typically, the vibrational analysis with periodic DFT follows the constrained geometry optimization, that is, stays in line with an assumption that the most important error caused by omitting long-ranged dispersion is the cohesive stress term. Therefore, the vibrational spectrum is modeled under a fictitious external pressure, equivalent to that arising from the cumulative sum of the long-range dispersion interactions. Nevertheless, the fictitious external pressure strongly depends on the studied unit cell and can be much larger; therefore, it may compensate some additional deficiencies arising from the applied methodology.⁵¹ Indeed, the stress-tensor calculations revealed that, as the PBE and rPBE calculations lead to a strong volume expansion (~ 28 and $\sim 56\%$, respectively), the constrained-cell equilibrium structures are under a large artificial pressure of $+0.98$ and $+3.80$ GPa, respectively. Nevertheless, it is not obvious how it affects the internal coordinates description.

The full set of coordinates coming from the X-ray diffraction and theoretical calculations—in the frame of both constrained and full optimization—has been given in the Supporting Information. Here, we present the percentage mean absolute errors of selected (non-hydrogen) interatomic distances delivered by each method. The results are collected in Figure 3.

Similarly to our previous findings,⁵¹ we may note that although the full relaxation with vdW corrections is a theoretically well-adjusted approach it does not provide an advantage over the

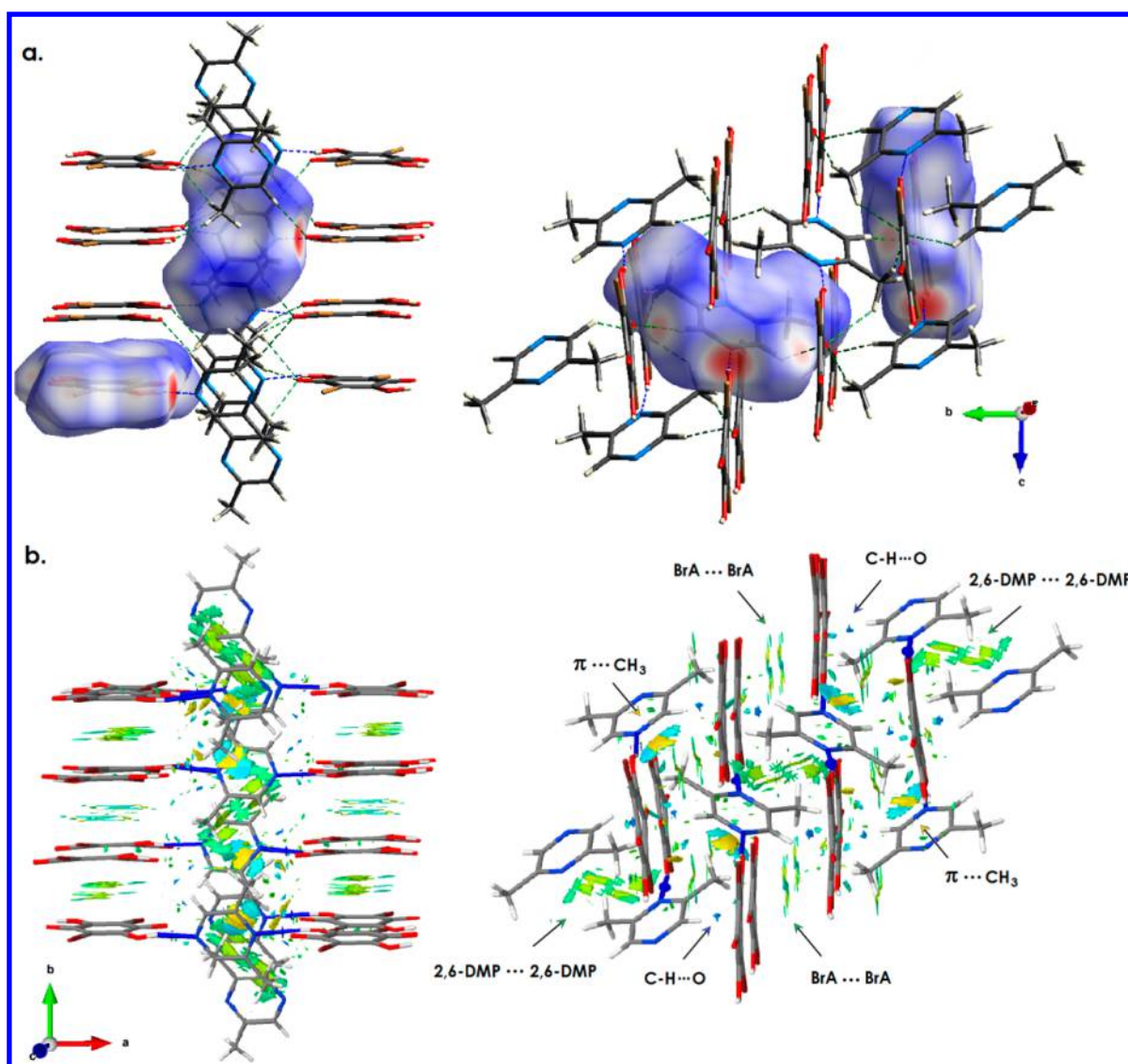


Figure 4. (a) Hirshfeld surface analysis of the intermolecular interactions in the BrA:2,6-DMP (1:1) co-crystal in the unit cell projection toward the crystallographic axes *c* and *a*, respectively. (b) Isosurface delivered by the reduced density gradient (RDG) analysis. The significantly attracting forces are colored in blue, whereas the repulsive interactions are shown in red. Weak van der Waals forces are marked in green and yellow, following their repulsive nature.

fixed-cell calculations. It has a practical consequence from the vibrational spectroscopy point of view, where we refer to the force constants. A slightly better performance of the Tkatchenko–Scheffler with respect to the Grimme scheme can be noticed here. As expected, the best relation between the experimental and theoretical internal distances is provided by “hard” rPBE. One could expect that the London forces inclusive parametrization of rPBE may be promising, which, however, has not been reported yet.

In conclusion, one can note that the most characteristic structural motifs are the supramolecular hydrogen-bonded 2,6-DMP:BrA chains. The polarization in each chain is neutralized by the neighboring one, arranged in the opposite direction as leading to the centrosymmetric phase. One may hence expect that the stabilizing forces will have a strong impact on the vibrational spectrum. In the further analysis, we will try to elucidate the nature of the intermolecular forces driving the discussed crystal packing.

Furthermore, we may conclude that the use of *ad hoc* dispersion corrections at the present level of their development does not necessarily provide a better internal coordinates description. Nevertheless, one should keep in mind that, while being more effective, the constrained-cell calculations are performed under a serious artificial stress, which has no physical justification and strongly depends on the studied system. In the present work, we will try to further focus on the relation of both schemes in modeling of the solid-state vibrational spectra over the entire spectral range.

Intermolecular Interactions. In order to better understand the nature of the crystallographic forces driving the molecular arrangement and crystal packing, the intermolecular interactions analysis was employed. The identification of the relative strength of competing interactions is an important task from the point of view of crystal engineering and possible doping or modifications of the material.

Therefore, the intermolecular forces were identified with the help of Hirshfeld surface^{52–56} and noncovalent interactions

Table 3. Hydrogen Bonds and Close Contacts in the BrA:2,6-DMP (1:1) Unit Cell as Found with X-ray Single-Crystal Diffraction (100 K) and Periodic DFT Calculations (0 K)^a

coordinate	X-ray	theory			
		Opt		Full-Opt	
		rPBE	PBE	PBE-TS	PBE-D2
H(2)⋯N(1) (Å)	2.0327	1.9072	1.8758	1.7757	1.6808
H(4)⋯N(2) (Å)	1.7825	1.5790	1.5593	1.5093	1.5168
O(2)⋯N(1) (Å)	2.8034	2.8296	2.8063	2.7261	2.6603
O(4)⋯N(2) (Å)	2.6257	2.5829	2.5747	2.5363	2.5393
∠O(2)–H(2)⋯N(1) (deg)	156.29	151.09	151.05	152.98	155.82
∠O(4)–H(4)⋯N(2) (deg)	156.15	157.97	157.93	158.13	157.91
H(8)⋯O(1) (Å)	2.4081	2.2177	2.1993	2.2320	2.2066
H(9)⋯O(1) (Å)	2.4467	2.3327	2.2989	2.3106	2.3269
∠C(8)H(8)⋯O(1) (deg)	170.84	171.72	169.89	163.79	162.88
∠C(9)H(9)⋯O(1) (deg)	128.77	125.37	128.10	128.39	124.75
BrA⋯BrA					
C(6)–Br1 (Å)	3.483	3.525	3.497	3.561	3.484
C(3)–Br2 (Å)	3.624	3.642	3.646	3.690	3.604
Br1– π (Å)	3.827	3.895	3.867	3.991	3.815
Br2– π (Å)	4.118	4.107	4.105	4.206	4.141
2,6-DMP⋯2,6-DMP (interplanar) (Å)	3.682	3.733	3.710	3.631	3.746
2,6-DMP⋯C(11)H ₃ (π ⋯CH ₃) (Å)	3.403	3.411	3.416	3.487	3.401
H ₃ C(11) ⋯ C(12)H ₃ (Å)	3.892	3.780	3.814	3.891	3.762
O(3)⋯H ₃ C(11) (Å)	3.500	3.479	3.437	3.412	3.385

^aThe theoretical data comes from the full- (Full-Opt) and constrained-cell (Opt) optimization.

(NCI) analysis.⁵⁷ The results are presented in Figure 4, while the parameters of hydrogen bonds and the most prominent close contacts are collected in Table 3.

Figure 4a represents the Hirshfeld surface plotted on the studied symmetry equivalent molecules. A Hirshfeld surface is a visualization tool, representing the interaction of the electron density of a selected molecule with that of the surrounding crystal structure. The surface is defined around the molecule at the point where contribution to the calculated electron density from the object and the surrounding is equal. The property projected here is the normalized contact distance (d_{norm}) from the surface to the nearest external atom (white, distance (d) equals the van der Waals distance; blue, d exceeds the van der Waals distance; red, d is less than the van der Waals distance). The surface was produced by the program Crystal Explorer.⁵⁸

By analyzing the figure, one can see the intense red spots around the hydrogen and nitrogen atoms engaged in the O–H⋯N hydrogen bonds. According to Table 3 and modern classification of the H-bond strength presented by Steiner,⁵⁹ the interactions can be classified as the moderate strength ones, since the ON distance found both experimentally and with DFT varies in the range of 2.54–2.83 Å. The O(2)–H⋯N(1) and O(4)–H⋯N(2) bonds were found to be nonequivalent, as the O⋯N distance on the CH₃ side of each 2,6-DMP molecule was found to be slightly longer. Both hydrogen bond angles are deviated from linearity, as found experimentally at 156(3)°.

Similarly, one can note bright red spots on the Hirshfeld surface over the C(8)–H and C(9)–H fragments. It suggests an existence of weak, dispersive hydrogen bonds of the C–H⋯O type. The H⋯O(1) distances found experimentally are equal to 2.41 (with the ∠C–HO⋯O angle ~171°) and 2.45 (with the ∠C–HO⋯O angle ~129°), respectively, being predicted by theory as slightly shorter ones (~0.2 Å).

The remaining interactions are less pronounced as corresponding to the light areas on the Hirshfeld surface. In order to get a more clear view on the nature of the weak vdW forces, the

second visual aid has been applied. The NCI analysis is a visualization index based on the electron density and its derivatives.⁵⁷ In general, it originates from the analysis of the reduced density gradient (RDG) at low densities. Differentiation between the noncovalent interactions is based on the analysis of the sign of the second density Hessian eigenvalue times the density. Such a value allows one to characterize interactions by means of the density strength and its curvature, while the results can be presented in the form of isosurfaces. The RDG analysis was performed using the pro-molecular densities, with a density cutoff of 0.25, and the color range +0.0175/–0.0175, using the NCI module implemented in JMOL.^{60,61}

The analysis of Figure 4b indicates the presence of moderate- and weak-strength hydrogen bonds, which are denoted as blue, localized areas. It also reveals the presence of significant forces between the molecular chains oriented in an opposite direction. These interactions give most striking, blurred contributions to the NCI isosurface and may be linked to the mutual compensation of the dipole moments.

A highly dispersive nature of the interactions can be, however, expressed by comparing the results of the full structural optimization by focusing on the cell constants b and c . The full relaxation with pure PBE overestimates the cell constants for ca. 21 and 8%, respectively. The corresponding BrA⋯BrA and 2,6-DMP⋯2,6-DMP interplanar contacts equal 3.896 and 4.245 Å, that is, giving a shift of 11.9 and 15.3%. The inclusion of the TS and D2 schemes significantly reduces the quoted errors down to +2.2; –1.4 and 0.0; +1.5%.

The nature of the quoted interactions is, however, not exactly clear. In each case, the molecules are significantly displaced from a sandwich orientation. Regarding the acid molecules, the BrA rings are slightly deviated from planarity, and the approximate BrA planes are twisted for about 5° to each other. The closest contacts are between the C(6)–Br(1) and C(3)–Br(2) ones, where the first one is about ~0.2 shorter than the second (3.483 vs 3.624 Å). It is interesting to note that the C(6) atom is under

the influence of the stronger hydrogen bond than C(3), which leads to a different electron density withdrawal. While at first glance one can identify the interactions as the displaced stacking type, the analysis suggests that there might be a significant contribution from the C–Br $\cdots\pi$ type halogen bonding.⁶² Such an assumption is supported by the geometric criterion,⁶² which suggests to observe such interactions at a Br $\cdots\pi$ distance smaller than 4.3 Å, which has been indeed confirmed by the data collected in Table 3.

The 2,6-DMP \cdots 2,6-DMP interactions of antiparallel molecules can be treated as displaced stacking forces. While the BrA \cdots BrA interactions are propagated to infinity, the antiparallel DMP molecules form dimer stacking moieties, being surrounded by the neighbors in a zigzag type manner toward the *b*-axis. While undergoing stacking from one plane, they are affected by $\pi\cdots\text{CH}_3$ attractions from another.

One of the CH₃ groups is more significantly affected by the crystal forces, being closer to heavy atoms as well as to the DMP surface. The differentiation between the C(11)H₃ and C(12)H₃ groups will be discussed further on.

Therefore, one may conclude that, in addition to the above-mentioned, moderate-strength hydrogen bonds, there are significant displaced stacking forces, affecting both acid and base molecules to a great extent and giving a strong stabilization of the crystal structure.

Solid-State NMR. The structural analysis was supplemented by high-resolution solid-state ¹³C NMR study, providing the “fingerprint” of the studied structure and underlying the nonequivalency of carbon atoms being affected by the intermolecular forces. In addition, ¹³C NMR allows one to verify the structural purity of the polycrystalline material.

In order to compare the calculated and experimental chemical shifts, the reference isotropic values were obtained with the help of the expression

$$\delta_{\text{calc}}^{\text{iso}} = \delta_{\text{ref}}^{\text{iso}} - a\delta_{\text{GIPAW}}^{\text{iso}} \quad (1)$$

as minimizing the RMSD errors between both data sets and introducing a scaling factor *a*.⁶³ The chemical shieldings assigned to the bromine- and hydroxyl-linked carbon atoms were excluded from the fitting procedure, as being most significantly deviated from the experimental values.

The recorded ¹³C CP/MAS NMR spectrum is given in Figure 5 against the results of the GIPAW calculations, carried out at both cell-constrained and fully relaxed structures. The full assignment of the ¹³C chemical shifts is given in Table 4.

The number of observed resonances corresponds to the number of carbon atoms in the asymmetric part of the unit cell. Since the system is locally highly symmetric (BrA, *C*_{2h}; 2,6-DMP, *C*_{2v}), most of the resonances are expected to be degenerated. Indeed, 12 signals are further combined into six pairs. GIPAW calculations provide an unambiguous assignment of the recorded resonances by inclusion of the crystal environment influence with the full-electronic accuracy. By analyzing Figure 5 and Table 4, one can note an excellent agreement between the experimental and theoretical values. The inclusion of the scaling factor in eq 1 allows one to directly compare the results obtained at each level of theory, while the differences are however rather negligible.

It was found that the methyl groups contribute to the NMR spectrum with the well-resolved signals found at 20 and 21 ppm. The ¹³C NMR spectrum reveals very slight but visible differentiation between the CH₃ fragments. The lowest resonance has been assigned to C(11)H₃, being less affected by crystal environment.

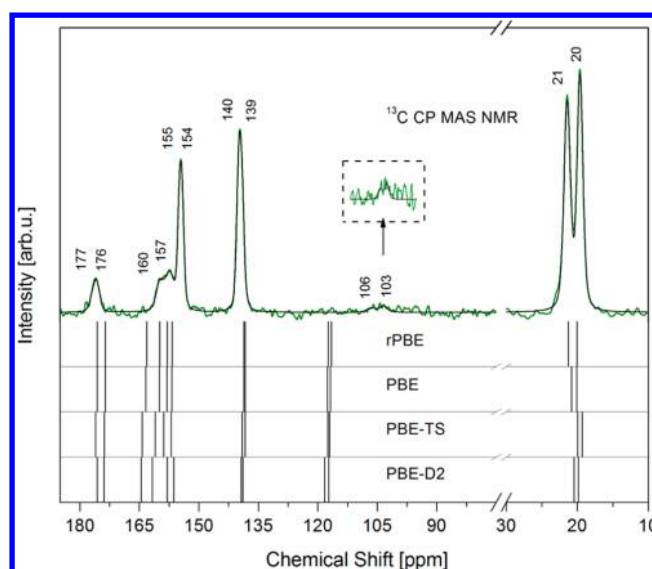


Figure 5. Experimental ¹³C CP/MAS NMR spectrum of BrA:2,6-DMP (1:1) against the theoretical (GIPAW) chemical shifts. The green line corresponds to the raw NMR signal, while the black line is the result of the Voigt function fitting. The theoretical results are given for both constrained (rPBE; PBE) and fully optimized (PBE-TS; PBE-D) crystal structures.

Table 4. Collection of Experimental (¹³C CP/MAS NMR) and Theoretical (GIPAW) Chemical Shifts (in ppm) for the BrA:2,6-DMP (1:1) Co-Crystal^a

¹³ C chemical shift δ (ppm)						
δ^{exp}	rPBE	PBE	PBE-TS	PBE-D2	molecular part	atom no.
177	175.6	175.7	176.0	175.6	¹³ C=O	C1
176	173.5	173.5	173.9	173.9		C4
160	163.2	163.4	164.3	164.5	¹³ C–OH \cdots N	C6
157	159.9	160.0	161.0	161.8		C3
155	157.9	158.1	158.9	158.0	N– ¹³ C–CH ₃	C7
154	156.7	156.8	157.0	156.3		C10
140	138.7	138.6	139.0	139.4	N– ¹³ C–H	C9
139	138.3	138.4	138.3	138.9		C8
106	117.4	117.6	117.1	117.2	¹³ C–Br	C2
103	116.6	116.8	117.5	118.3		C5
21	21.3	20.8	20.0	20.5	¹³ CH ₃	C12
20	20.1	20.1	19.3	19.9		C11
$\delta_{\text{ref}}^{\text{iso}}$	169.0	165.4	165.7	165.4		
<i>a</i>	0.97	0.96	0.96	0.96		

^aThe theoretical results are given for both constrained (rPBE; PBE) and fully (PBE-TS; PBE-D) optimized crystal structures. The reference ($\delta_{\text{ref}}^{\text{iso}}$) and scaling factor (*a*) values are given for each model. The atom labeling is consistent with Figure 2a.

The barely detectable resonances were recorded at 103 and 106 ppm (and predicted around 117 ppm), as corresponding to the bromine-linked carbons. Their resolution is completely ruined due to the presence of the residual dipolar coupling between the carbon atoms and the quadrupolar nuclides. This effect has been extensively studied by Terskikh et al.⁶⁴ We have also faced a similar failure of the GIPAW approach in the case of the complex of bromanilic acid with tetramethylpyrazine and assigned the source of the predicted chemical shift deviation to the relativistic effects.⁶⁵

Due to the coupling of the ^{14}N and ^{13}C nuclei, one can observe a fine structure in the ^{13}C NMR spectrum. The upper pairs of nearly degenerated signals were found at 138, 139 and 154, 155 ppm, which are due to the nitrogen-linked carbons. The lower signals are due to the C–H atoms, while the upper ones are linked to the methyl groups.

The coupling of the ^{13}C nuclei to the ^{16}O gives lowering of the band intensity and results in the set of resonances observed around 160 and 175 ppm. It is worth mentioning that the quoted bands indicate the protonation state and the hydrogen bonding. Then, the lower signals observed at 157 and 160 ppm are assigned to the C–OH fragments. This visible difference of ~ 3 ppm—properly predicted by theory—has been assigned to the hydrogen bonds of slightly different strength. The proton withdrawal in the stronger H-bond manifests in the signal found at 160 ppm.

Finally, the top signal in the NMR spectrum is assigned to the $^{13}\text{C}=\text{O}$ fragments. Since the weak C—H \cdots O(1) interactions were identified in the crystal structure, the upper signal has been assigned to the carbon atom associated with this weak dispersion-type hydrogen bond.

In summary, one can conclude that the ^{13}C NMR study confirmed a high purity of the polycrystalline sample. An excellent agreement between the GIPAW results and the experimental data suggests that the studied structure is a highly ordered system. Since there is a clear differentiation between the C=O and C–OH groups, without any satellite bands or anomalous band broadening, one can expect that the proton is highly localized as postulated above and there are no tautomeric contributions present. The related C–OH resonances clearly differentiate the hydrogen-bond strength and reflect the nonequivalency of methyl fragments which are to be analyzed in detail below.

Vibrational Analysis. General Discussion. In search of the interactions—structure interplay, the vibrational spectroscopy remains the most powerful tool. Here, the vibrational response has been thoroughly analyzed by referring to both optical and neutron spectroscopy techniques. Such a combination provides a direct insight into the environmental and structural factors driving the studied phase, as referring both to the high- and low-energy vibrational excitations. By combining infrared and Raman spectroscopy, we are able to directly probe the localized internal modes, which differ in their polarity. In addition, the use of inelastic neutron scattering gives complementary information about the hydrogen dynamics. Finally, employing terahertz optical spectroscopy gives a chance to underline the lattice vibrations, which are directly associated with the intermolecular forces of weak strength.

In the studied case, the crystal structure with $Z = 4$ implies that the system gives rise to 360 zone-center phonons, distributed along the symmetry species as follows: $\Gamma_{\text{C}_{2h}} = 90A_g + 90B_g + 90A_u + 90B_u$. The *gerade* (A_g ; B_g) modes are Raman active, while the *ungerade* (A_u ; B_u) phonons give a break of the inversion symmetry, being allowed to be observed in infrared/terahertz spectroscopy. Among 360 species, 312 vibrations are the internal modes of BrA (144) and 2,6-DMP (168), respectively. The remaining 48 external vibrations engage the hydrogen bond related degrees of freedom along with 24 lattice vibrations due to molecular rotations and translations. Twenty-one lattice vibrations are optically active, while three acoustic modes of zero frequency at the Γ -point correspond to the translation in the z (A_u), x , and y ($2B_u$) directions, respectively.

The studied system is an illustrative example of the mutual exclusion rule, where 177 and 180 vibrations are allowed to be observed in IR and Raman, respectively. However, the polar nature of some of the discussed vibrations can limit the direct complementarity of both techniques. In principle, the vibrational frequencies can be affected by a coupling of phonon modes with a macroscopic electric field. In such a case, an infrared active mode has an associated dipole moment, which changes the related energy of a phonon in the presence of a long-range dipole–dipole coupling. Such coupling is always present in the IR spectra of crystalline materials and manifests itself in a frequency difference between the longitudinal and transverse optical modes, known as LO–TO splitting. For the centrosymmetric structures, the mutual exclusion rule makes the polar modes forbidden in Raman spectroscopy.⁶⁶ Since the related modes do not lead to the presence of a macroscopic electric field in the lattice, only transverse optical (TO) modes would give the contribution to the Raman spectrum.

Moreover, for a noncubic single crystal, the magnitude of the LO–TO splitting depends on the $q \rightarrow \Gamma$ approaching direction, and the longitudinal optical (LO) modes change their frequency continuously as an angular function. Then, for a polycrystalline sample, there can be a range of frequencies associated with LO modes, as multiple grain orientations sample all possible frequencies. Furthermore, the LO frequency also depends on the grain size and shape. Therefore, if the crystallite size is comparable with the wavelength of light, then the particles act as an optical cavity and further interact with the LO modes to change the vibrational spectrum.⁶⁷

Generally, in the case of noncentrosymmetric polar materials, the Raman spectra consist of sharp peaks and the background bands originating from the LO modes.

In addition to the optical vibrational spectroscopy, we have applied the inelastic neutron scattering (INS) as going beyond the Γ point vibrations. In principle, the observed intensity, $S(Q, \omega_i)$, of the i th mode is proportional to the factor

$$S(Q, \omega_i) \propto Q^2 U_i^2 \exp(-Q^2 U_{\text{total}}^2) \sigma_{\text{inc}} \quad (2)$$

where U_i is the amplitude of atomic motion upon particular vibration \hat{u}_i . The exponential term is known as the Debye–Waller factor and U_{total}^2 is the mean square displacement of the molecule, whose magnitude is in part determined by its thermal motion, which can be further reduced by cooling the sample. The incoherent neutron scattering cross section of an atom (σ_{inc}) is an isotope specific property which is independent of its chemical environment. Since the cross section value for hydrogen is far greater than that of all other elements, the INS spectrum emphasizes the modes that involve substantial hydrogen motion;⁶⁸ therefore, this technique is more specific than IR and RS.

In contrast to the optical vibrational spectroscopy, INS does not follow the optical symmetry selection rules, as all modes are, in principle, allowed and their probability depends mainly on the displacement amplitude and the incoherent neutron scattering cross section (σ_{inc}) of an atom.⁶⁸ While none of the vibrations are forbidden by symmetry, also polar modes are equivalently allowed, then, the LO modes can also contribute to the spectrum. However, while a rather lower-wavenumber range is practically accessible to INS, such effects are not so prominent in the case of molecular systems as in infrared spectroscopy.

Born Charge Contributions. In principle, the magnitude of the LO–TO splitting is associated with the dielectric permittivity and the dimensionless Born charge tensors (also known as the

atomic polar tensor, APT), giving information about the response of the system to perturbations, particularly those that create an electric field. The dynamical charge tensor of an ion may be defined as the partial derivative of the macroscopic polarization with respect to a periodic displacement of all its periodic images under conditions of zero external field. Therefore, it can be defined as $Z_{k,\alpha\beta}^* = (\Omega/e)\partial P_\alpha/\partial u_{k,\beta}$, where P_α is the component of the polarization in direction α , $u_{k,\beta}$ is the displacement of atom k in direction β , while Ω is the primitive cell volume, and e stands for the charge quantum. The polar character of a system is known to be connected with the presence of anomalously large Born charges. It has already been shown that such a quantity can be attributed to the microscopic underpinnings of ferroelectric behavior in organic solids.^{69,70}

In order to estimate the magnitude of the discussed long-range dipole coupling in the present case, a further theoretical insight has been given. The qualitative view on the APT tensors has been illustrated in the form of ellipsoids in Figure 2a. One can note that the largest and most anisotropic contributions come from the hydrogen-bonded BrA moieties, while the 2,6-DMP contributions are negligible here. The full collection of the diagonal components of the Born charge tensors can be found in the Supporting Information. Here, we present the quantitative analysis (see Table 5), where the dominating xx diagonal components are given against the tensor derived quantities, namely, the mean dipole derivative (\bar{p}), the effective charge (χ), and the tensor anisotropy (β^2).⁷¹ The mean dipole derivative is evaluated as the arithmetic mean of the three diagonal elements, while the effective charge is equal to the square root of 1/3 the sum of squares of all nine tensor elements. Finally, the tensor anisotropy is defined in terms of the above two invariants as $\beta^2 = 9/2(\chi^2 - \bar{p}^2)$.

In order to give a reference, one can refer to the CH₃ groups, where one can find the following parameters for the carbon and hydrogen atoms, respectively: $\bar{p} = 0.15$; $\chi = 0.32$; $\beta^2 = 0.35$ and $\bar{p} = 0.07$; $\chi = 0.15$; $\beta^2 = 0.09$. The results collected in Table 5 indicate anomalously large values of the quoted quantities.

If comparing the selected levels of theory, one can note a clear tendency, where the calculated values are generally increasing in the following order: rPBE < PBE < PBE-TS < PBE-D2.

The analyzed quantities reflect the presence of specific interactions in the system. As one can note, the most prominent effective charges, with a huge tensor anisotropy, are associated with the C=O—H...N bonded atoms, being highly directional toward the H-bonding, that is, having the generally largest xx tensor components. The further analysis differentiates the hydrogen-bond strength, since the shorter O...N distance leads to the larger proton withdrawal and increase of the C—O bond strength and its polarization.

One can note an opposite effect if comparing the lone-paired carbonyl groups, where the one engaged in weak C=O...H—C attractive interaction gives lower values of the analyzed components.

As a consequence, one can expect that the modes resulting in displacement of the discussed atoms will give a strong infrared response, being significantly affected by the long-range dipole coupling. By analyzing the Born charge tensors, one can also expect that its magnitude influence will depend on the applied methodology. In order to provide further insight, the infrared spectroscopy across the entire spectral range has been used. The long-range dipole influence has been probed by adding the nonanalytic term to the dynamical matrix in the hydrogen bond

Table 5. Dominating xx Diagonal Components of the Born Charge Tensor (Z^*) in the BrA:2,6-DMP (1:1) Complex as Calculated by Plane-Wave DFT at the GGA/1050 eV Level of Theory^a

atom	molecular fragment	rPBE			PBE			PBE-TS			PBE-D2		
		Z^*	\bar{p}	χ	β^2	Z^*	\bar{p}	χ	β^2	Z^*	\bar{p}	χ	β^2
C ₁	C=O...H—C	2.15	1.31	1.55	3.06	2.19	1.33	1.57	3.15	2.23	1.31	1.58	3.46
O ₁		−2.05	−1.18	1.35	1.87	−2.09	−1.21	1.37	1.94	−2.13	−1.21	1.39	2.10
C ₄	C=O	2.33	1.36	1.67	4.27	2.38	1.37	1.70	4.50	2.43	1.36	1.71	4.81
O ₃		−2.23	−1.23	1.45	2.70	−2.29	−1.25	1.48	2.86	−2.34	−1.26	1.51	3.05
C ₃	C=O—H...N (weaker)	1.18	0.58	1.33	6.43	1.21	0.60	1.34	6.51	1.28	0.64	1.39	6.87
O ₂		−2.09	−1.19	1.56	4.52	−2.18	−1.22	1.60	4.80	−2.37	−1.28	1.70	5.71
H ₂		1.98	0.92	1.23	2.92	2.07	0.95	1.28	3.24	2.31	1.02	1.41	4.29
N ₁		−0.89	−0.62	0.67	0.29	−0.89	−0.62	0.67	0.30	−0.96	−0.63	0.70	0.40
C ₆	C=O—H...N (stronger)	1.23	0.66	1.40	6.82	1.26	0.69	1.42	6.90	1.32	0.72	1.45	7.12
O ₄		−2.64	−1.43	1.90	6.94	−2.71	−1.46	1.94	7.23	−2.81	−1.49	2.01	8.14
H ₄		2.93	1.21	1.77	7.56	3.01	1.24	1.83	8.06	3.12	1.28	1.91	8.98
N ₂		−1.20	−0.45	0.76	1.70	−1.22	−0.45	0.77	1.77	−1.27	−0.46	0.81	1.98

^aThe data are reported along with the tensor derived quantities (see the text for details), namely, the mean dipole derivative (\bar{p}), the effective charge (χ), and the tensor anisotropy (β^2). The theoretical structures refer to the fixed-cell (PBE; rPBE) and full-optimization under atmospheric pressure (PBE-TS; PBE-D2). The collected charges are given in units of $|e|$. The atom labeling is consistent with Figure 2a.

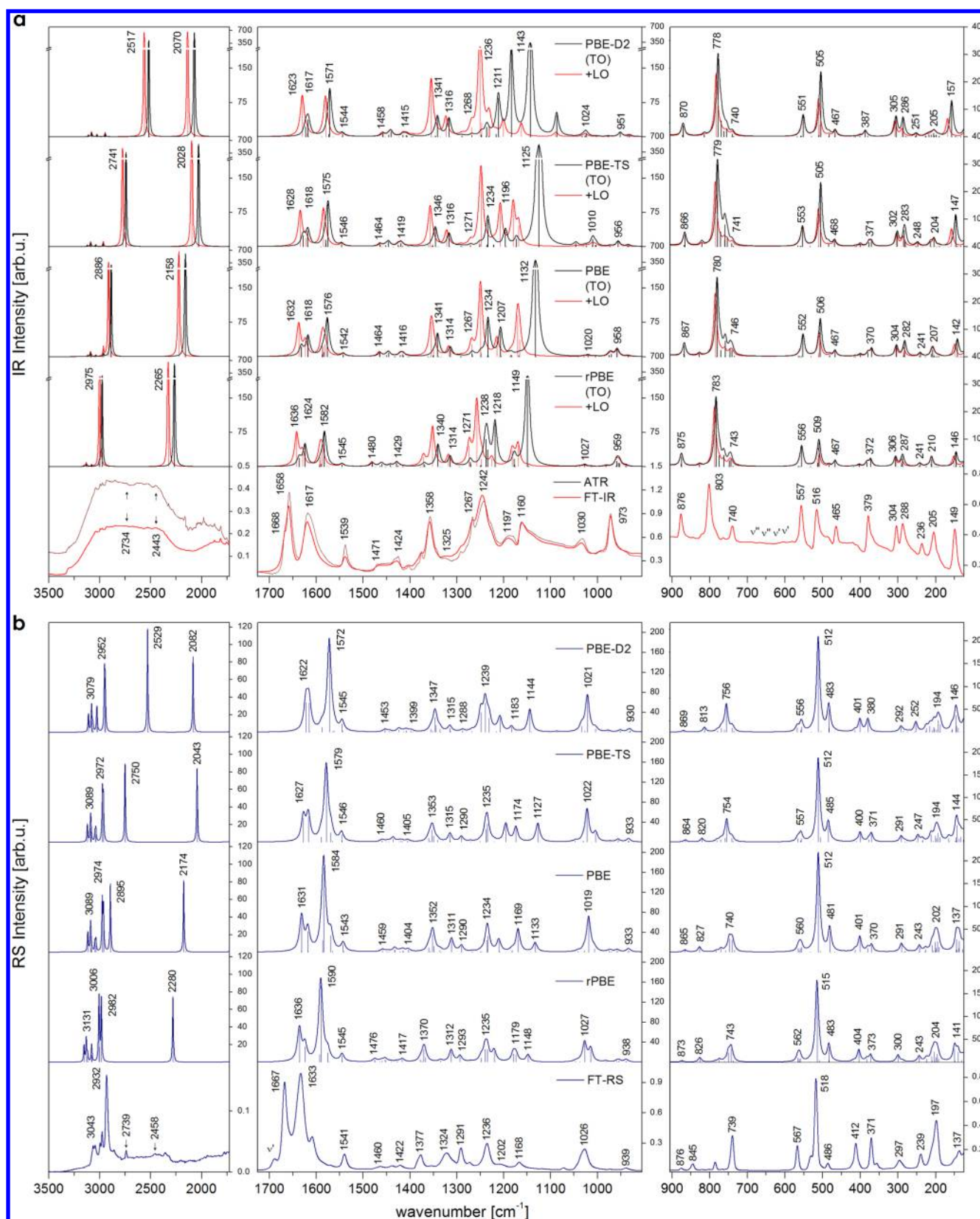


Figure 6. (a) Experimental transmission (red) and attenuated total reflection (dark red) infrared and (b) Raman spectra of BrA:2,6-DMP (1:1) as divided into 3500–1750, 1750–900, and 900–125 cm^{-1} wavenumber areas. The experimental spectra are presented against the results of linear-response calculations. The theoretical data are taken from both constrained (rPBE; PBE) and fully (PBE-TS; PBE-D) optimized crystal structures. The red and black curves in the theoretical IR spectra correspond to the results obtained both with (+LO-TO) and without (TO) inclusion of the long-range dipole coupling, where the wavenumber labeling corresponds to selected TO modes. Raman spectra refer to the TO components.

Table 6. Collection of Experimentally Observed FT-IR, FT-RS, and INS Wavenumbers (ν , cm^{-1}) for the BrA:2,6-DMP (1:1) Complex along with a Tentative Band Assignment^a

IR		RS		IR		RS		IR		RS		INS		Tentative Mode Assignment			
Theory PBE Γ				Experiment		Theory PBE Γ				Experiment		Experiment					
S.	Δ^{LO}	TO	S.	TO	298K	S.	Δ^{LO}	TO	S.	TO	298K	10K	v [cm ⁻¹]				
	v [cm ⁻¹]			v [cm ⁻¹]			v [cm ⁻¹]										
	v [cm ⁻¹]			v [cm ⁻¹]			v [cm ⁻¹]										
			A _g	3116	3065				B _u	0	867	A _g	865	876	876 ^{Ag}	$\omega(\text{C}_{(8)}\text{H}; \text{C}_{(9)}\text{H})^{\text{DMP}}; \rho(\text{CH}_3)^{\text{DMP}}$	
			A _g	3089	3043				B _g	828			851	826 ^{Au}		$\nu\text{Br-C}^{\text{DMP}}; \beta\text{BrA}^{\text{(ring, Trigonal, 12)}}$	
			A _g	3046	2996				B _u	0	828	A _g	827	844	845		
			A _g	3036	2975				B _u	5	780	A _g	782	803	802	802 ^{Bu}	$\beta\text{BrA}^{\text{(ring, Trigonal, 12)}}; \delta\text{O}_{(4)}\text{H}_{(4)}\cdots\text{N}_{(2)}$
			A _g	2974	2937				B _u	0	770					$\delta\text{O}_{(2)}\text{H}_{(2)}\cdots\text{N}_{(1)}$	
			A _g	2962	2928				B _u	0	770			784			$\gamma\text{BrA}^{\text{(ring, 4, Puckering)}}$
B _u	26	2886	A _g	2895	2734	2739			B _g	770				785			$\delta(\text{C-X})^{\text{BrA(Twist mode)}}; \gamma\text{DMP}^{\text{(ring, 4, Puckering)}}$
B _u	64	2158	A _g	2174	2443	2458			B _u	1	759	B _g	758	765		774 ^{Bu}	
B _u	6	1632			1668				B _u	1	746	B _g	747			741 ^{Bg}	
B _u	5	1618	A _g	1618	1658	1667			A _g	748				748			$\gamma\text{DMP}^{\text{(ring, 4, Puckering)}}$
			A _g	1587	1649				B _u	1	746	B _g	747				
			B _g	1585	1641				B _u	0	741			740			$\gamma\text{DMP}^{\text{(ring, 4, Puckering)}}$
			A _g	1584	1633				A _g	740				739			
B _u	5	1576	A _g	1569	1617	1609			A _u	0	561	A _g	562	568		564 ^{Ag}	$\delta(\text{NC}=\text{C})^{\text{DMP (ring, 6b)}}$
			B _g	1565		1569			A _u	0	552	B _g	560		567		$\gamma\text{BrA}^{\text{(ring, 17b)}}$
			B _g	1543		1541			B _u	0	531	A _g	532	534	532	533 ^{Ag}	$\gamma\text{DMP}^{\text{(ring, 16a)}}$
A _u	0	1542			1539												
B _u	1	1464	B _g	1459	1471	1472			A _g	512				518			$\delta(\text{C}=\text{C}=\text{C})^{\text{BrA(ring, 6a, Quadratic)}}$
			B _g	1450		1464			B _u	3	506			516			$\beta\text{BrA}^{\text{(ring, Trigonal, 12)}}; \delta(\text{C}=\text{C}-\text{O})^{\text{BrA}}; \delta(\text{C}=\text{C}=\text{O})^{\text{BrA}}$
A _u	0	1445	A _g	1445	1462	1460			A _u	0	506	B _g	506			502 ^{Au}	
			A _g	1422		1437			B _g	481			487	486			$\gamma\text{BrA}^{\text{(ring, 10a)}}$
			B _g	1421		1425			B _u	0	467			465			$\gamma\text{DMP}^{\text{(ring, 16b)}}$
A _u	0	1415	A _g	1416	1424	1422			B _u	0	417	B _g	415			415 ^{Bg}	$\delta(\text{C-X})^{\text{DMP(Twist mode)}}; \delta(\text{C}-\text{C}-\text{CH}_3)^{\text{DMP}}$
			B _g	1414		1418			A _g	401				412			$\delta(\text{C}=\text{C}=\text{C})^{\text{BrA(ring, 6b)}}$
A _u	0	1403	A _g	1404	1409	1413			B _g	401				410			$\nu\text{H}_{(4)}\cdots\text{O}_{(1)}; \delta(\text{CCO})$
B _u	0	1361	A _g	1360	1384	1384			B _u	0	380	A _g	381	379		384 ^{Ag}	$\nu\text{H}_{(2)}\cdots\text{O}_{(3)}; \delta(\text{CCO})$
B _u	4	1351	A _g	1352	1376	1377			A _u	0	304	B _g	304			305 ^{Au}	$\nu(\text{C-Br})^{\text{BrA}}; \delta(\text{C}=\text{C}=\text{O})^{\text{BrA}}; \delta(\text{C}=\text{C}-\text{O})^{\text{BrA}}$
B _u	9	1341	A _g	1336	1358	1356			B _u	2	304	A _g	304	304	306		
B _u	3	1314	A _g	1311	1325	1324			A _g	291				297			$\delta(\text{N-C-CH}_3)^{\text{DMP}}$
A _u	0	1292	A _g	1290	1291	1291			B _u	1	282	B _g	281	288	287	289 ^{Bu}	$\delta(\text{N-C-CH}_3)^{\text{DMP}}; \gamma\text{BrA}^{\text{(ring, 10b)}}$
B _u	2	1267			1267				A _u	0	243	B _g	244			233 ^{Au}	$\gamma\text{DMP}^{\text{(HCNC + CCNC)}}$
			A _g	1267		1273			B _u	0	240	A _g	243	236	239		
B _u	16	1233	A _g	1234	1242	1236			B _u	0	226	A _g	226			189 ^{Au}	$\tau(\text{C}_{(12)}\text{H}_3)^{\text{DMP}}$
B _u	8	1207	A _g	1211	1228	1234			A _g	210				207	211 ^{Ag}		$\gamma\text{DMP}^{\text{(CCNC + CCNC) + \gamma(C_{(12)}H_3)}}; \delta(\text{C-X})^{\text{BrA(Twist mode)}}$
A _u	0	1183			1197				A _u	0	207			205			$\gamma\text{DMP}^{\text{(CCNC + CCNC) + \gamma(C_{(12)}H_3)}}; \gamma\text{BrA}^{\text{(ring, 11)}}$
			A _g	1169	1202				A _g	202				197			$\tau(\text{HC-N-CH})^{\text{DMP}}; \gamma\text{DMP}^{\text{(CCNC - CCNC) + \gamma(C_{(12)}H_3)}}; \gamma\text{BrA}^{\text{(ring, 11)}}$
B _u	3	1167			1186				B _u	0	197			194			$\tau(\text{HC-N-CH})^{\text{DMP}}; \gamma\text{BrA}^{\text{(ring, 11)}}$
B _u	34	1132	A _g	1133	1160	1168			A _u	0	196	A _g	195				$\tau(\text{HC-N-CH})^{\text{DMP}}; \delta(\text{C}=\text{C}-\text{C})^{\text{BrA(ring, 6b, Quadratic)}}; \nu(\text{Br}\cdots\text{Br})$
A _u	0	1041	A _g	1042	1073	1072			B _u	0	191			182			$\tau(\text{HC-N-CH})^{\text{DMP}}; \delta(\text{C}=\text{C}-\text{C})^{\text{BrA(ring, 6b, Quadratic)}}; \nu(\text{Br}\cdots\text{Br})$
B _u	0	1020	A _g	1019	1030	1026			B _u	4	146	A _g	146			154 ^{Bu}	$\gamma\text{BrA}^{\text{(C-O - C-O)}}; \text{DMP lib. } \angle\text{bc}$
			A _g	1006		1018			A _u	142		B _g	145		149		$\gamma\text{BrA}^{\text{(C-O - C-O)}}; \text{DMP lib. } \angle\text{bc}$
B _u	1	975			994				B _u	2	142			149			$\delta\text{BrA}^{\text{(ip} \rightarrow \text{BrC604H2} \leftarrow \text{)}}; \text{DMP lib. } \angle\text{bc}$
B _u	0	958	A _g	958	972	972			A _u	0	134	B _g	138			141 ^{Bg}	$\text{DMP lib. } \angle\text{bc}; \tau(\text{C}_{(11)}\text{H}_3)^{\text{DMP}}; \gamma\text{BrA}^{\text{(C-O - C-O)}}$
B _u	0	934			938				A _g	137				137			$\text{DMP lib. } \angle\text{bc}; \tau(\text{C}_{(11)}\text{H}_3)^{\text{DMP}}; \gamma\text{BrA}^{\text{(C-O - C-O)}}$
			B _g	934	939												

^aThe experimental data are presented against the results of zone-center lattice dynamics calculations (fixed-cell PBE/1050 eV data). The symmetry (S) is noted for each transverse optical (TO) mode, while the frequencies of longitudinal components (LO) are presented as a wavenumber difference (Δ^{LO}) with respect to a given *ungerade* TO mode. See the Supporting Information for an extended version of the table.

direction, that is, giving the maximum-frequency LO contributions.

Band Assignment. The experimental FT-IR and FT-RS spectra have been presented against the results of the theoretical calculations in Figure 6a and b, respectively. The detailed assignment of the spectral features has been collected in Table 6 as referring to standard PBE calculations. For the full collection of the LO and TO wavenumbers, we refer the reader to the Supporting Information. The subsequent discussion is devoted to the most prominent spectral features, being divided into several spectral areas, explored by complementary experimental techniques.

We hence provide a possibly full assignment of the vibrational features in the model system, representing the anilic acid-pyrazine-type base conjugates, which are promising from the point of view of functional materials.

4000–1750 cm^{-1} . One should note that the highest wavenumber range cannot be restored properly using harmonic approximation as being covered by large-amplitude $\nu(\text{X-H})$ vibrations. Nevertheless, as has been earlier revealed by Balan et al.,⁷² the systematic deviation of GGA DFT in description of the potential energy surface of the stretching coordinates leads to the lucky cancelation of errors due to anharmonicity. Therefore, despite the theoretical deficiency of harmonic approximation, some general support can be provided here.

The anharmonicity of the stretching modes has several effects specific in character for hydrogen bonds. Particularly, it is commonly accepted that the anharmonicity gives rise to the coupling phenomena of the $\nu(\text{X-H})$ vibrations with the low frequency modes, mainly of the bridge stretching and modes into which the bridge atoms contribute.⁷³ This problem has been formulated theoretically by Marechal and Witkowski^{74,75} and further developed by by Wójcik and Witkowski to introduce the Fermi resonance effects.^{76,77} Such a coupling leads to the substructure of the $\nu(\text{X-H})$ bands and large broadening due to *quasi* Franck–Condon progression. Therefore, the related IR absorption bands usually result from the relaxation of the excited vibrational levels through the coupling with the low frequency internal vibrations which further interact with lattice phonons.

By analyzing both the transmission and ATR spectra presented in Figure 6a, one can observe a broad band covering the spectrum in the range of 2200–3300 cm^{-1} . The large contribution from the $\nu(\text{O-H})$ modes completely covers the weak $\nu(\text{C-H})$ bands. One can note the two broad components with the centers of gravity found around 2900 and 2500 cm^{-1} , where the former and the latter can be assigned to the weaker ($\text{O}(2)\text{H}\cdots\text{N}(1)$) and stronger ($\text{O}(4)\text{H}\cdots\text{N}(2)$) hydrogen bonds, respectively. Both modes undergo a visible coupling to the slow $\text{O}\cdots\text{N}$ bridge stretchings, resulting in the substructure formed by the progression components, separated by ca. $\sim 80\text{--}100\text{ cm}^{-1}$. Due to a large band broadening, it is difficult to precisely define the $\nu(0 \rightarrow 1)$ position of each band.

However, it is reasonable to assign the $0 \rightarrow 1$ transitions to the lower components found at 2739 and 2458 cm^{-1} , respectively. By comparing the wavenumbers with the results of the theoretical calculations, one can observe a visible, lucky cancelation of errors due to anharmonicity, with the wavenumber lowering in the following order: $\text{rPBE} > \text{PBE} > \text{PBE-vdW}$. The fixed-cell PBE calculations predict the TO components at 2886 and 2158 cm^{-1} with a large LO–TO splitting, reaching 64 cm^{-1} in the case of the stronger hydrogen bond, which further affects the experimental spectrum. The theoretical calculations predict a huge intensity of the related bands, which however is damped in

the experimental spectrum, where the intensity is distributed over the entire range of coupled modes.

If referring to the Raman spectrum, one can clearly identify the $\nu(\text{CH})$ stretchings distributed over the range of $\sim 3100\text{--}2850\text{ cm}^{-1}$. In contrast to IR, one can note a background band outstretched through $\sim 2200\text{--}3300\text{ cm}^{-1}$. It is difficult to underpin the nature of such large intensity damping. Alternatively, one can assign the background band to the LO wing, which might contribute to the local break of symmetry due to excitation of the highly energetic infrared modes undergoing coupling to the lattice vibrations.

The spectral analysis reveals two relatively sharp bands found at 2739 and 2458 cm^{-1} . Therefore, it is reasonable to assign them to the $0 \rightarrow 1$ transitions, confirming a proper assignment of the above-discussed IR counterparts. Such assignment is strongly supported by PBE-D2 calculations.

1750–925 cm^{-1} . As in the case of the $\nu(\text{X-H})$ range, a visible red shift of the calculated wavenumbers was found in the order $\text{rPBE} > \text{PBE} > \text{PBE-TS} > \text{PBE-D2}$, that is, in agreement with the above-described hierarchy of accuracy in the internal coordinates description. Recently, by using the full electronic calculations⁷⁸ (PBE/6-31++G(d,p)), we were able to show that such systematic error partially comes from the use of norm-conserving pseudopotentials.⁷⁹ In line with our previous findings,⁶⁵ the fixed-cell PBE calculations call for the use of a uniform scale factor of ca. 1.015, for the medium-wavenumber range. Nevertheless, all the wavenumbers reported here were left unscaled.

By analysis of Figure 6a, one can note that, except for the systematic wavenumber underestimation, an excellent agreement between the experimental and theoretical spectra has been achieved in the case of both IR and Raman spectra, allowing for a precise assignment of the vibrational features. In contrast to the Raman spectrum, which is free of such effects, a very prominent influence of the above-discussed long-range dipole coupling has been found in the IR spectrum, giving a serious broadening of some of the experimental bands and introducing the band shape asymmetry.

As can be clearly seen in Figure 6a, the long-range dipole coupling not only affects the wavenumber of each absorption band, but—what is more—it very significantly affects their intensities (see Table S3 in the Supporting Information for the quantitative analysis). As a result, it is impossible to precisely define the TO wavenumbers in the IR spectrum. In line with the above presented Born charge analysis, the magnitude of the LO–TO splitting directly follows the order $\text{rPBE} < \text{PBE} < \text{PBE-TS} < \text{PBE-D2}$.

While it is impossible to quantitatively compare the IR intensities relations on the basis of a powder sample, the qualitative view on Figure 6a clearly suggests an overestimation of related effects by the vdW corrected schemes. The band asymmetry is directed toward lower wavenumbers, while the wavenumbers of the LO components are generally shifted in the opposite direction.

By analyzing the spectra in more detail, one can find the set of bands covering the range of $\sim 1700\text{--}1600\text{ cm}^{-1}$, which is typical for the carbonyl stretchings. The upper band is due to the $\nu(\text{C=O})$ vibrations, mixed with the BrA $\nu(\text{C=C})$ modes, and hence can be clearly observed with both IR and RS. There is about 10 cm^{-1} separation between the $\nu(\text{C=O})$ modes, reflecting the $\text{C-H}\cdots\text{O}(3)$ attracting interactions. Similarly, the lower band is due to 2,6-DMP and BrA ring stretchings, giving a strong Raman response. Since the modes are mixed to the in-plane $\delta(\text{O-H}\cdots$

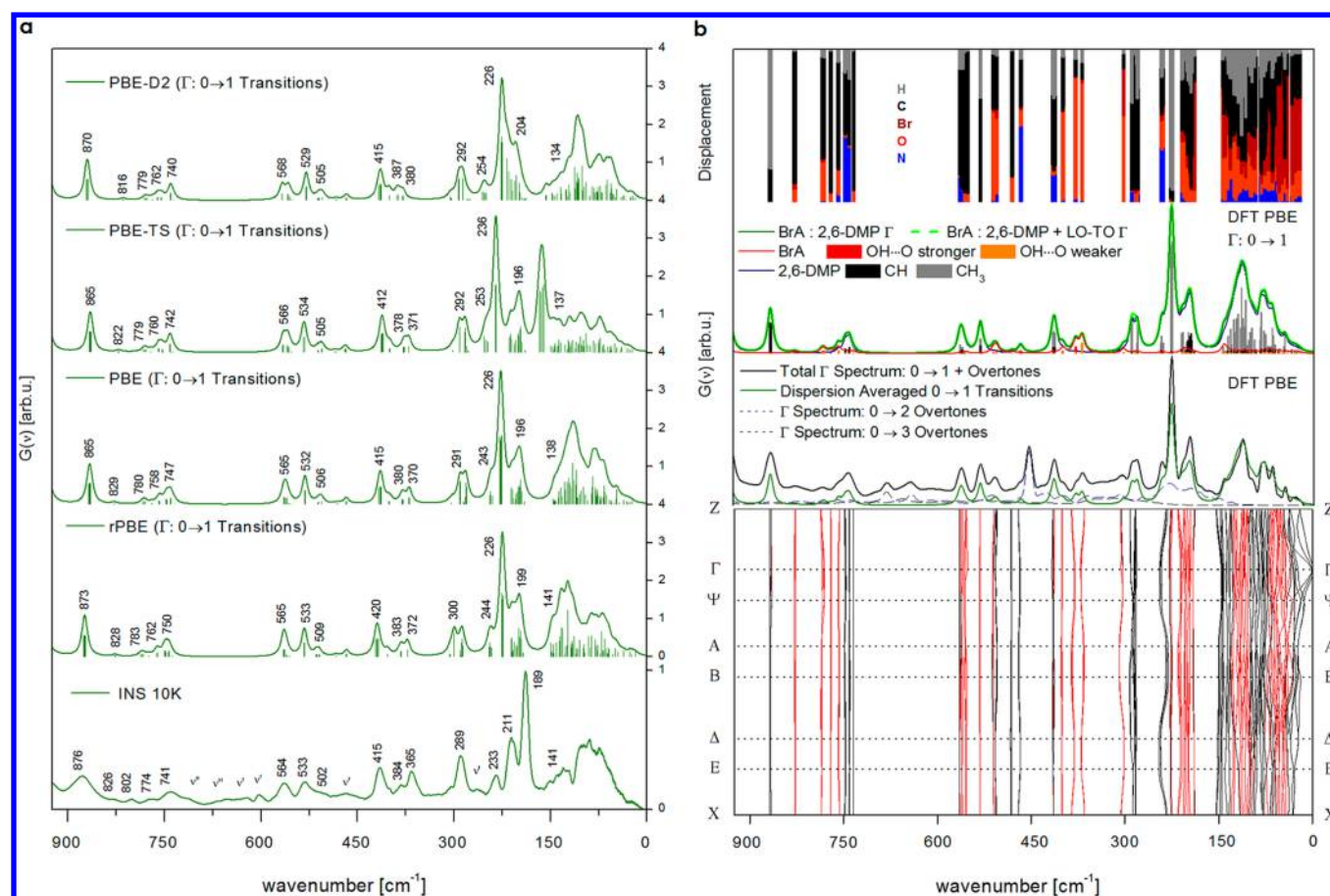


Figure 7. (a) Experimental (NERA 10 K) and theoretical ($0 \rightarrow 1$ transitions) INS spectra of BrA:2,6-DMP (1:1), presented in the range below 925 cm^{-1} . The theoretical spectra are given for both constrained (rPBE; PBE) and fully (PBE-TS; PBE-D) optimized crystal structures. (b) The representative PBE results are presented in more details, by providing phonon dispersion curves along with the vibrational density of states (VDOS) decomposed into partial VDOS contributions of each molecular fragment. In addition, the dispersion averaged spectrum is given along with the total Γ -point spectrum including the overtone contributions.

N) bendings, they contribute to the IR spectrum. The related IR band is visibly, asymmetrically broadened on account of the polar effects.

While the range of $\sim 1550\text{--}1375 \text{ cm}^{-1}$ is mainly covered by the CH bendings in DMP, the $\nu(\text{C--O})$ stretching coupled to the in-plane $\delta(\text{O--H}\cdots\text{N})$ deformation of a weaker H-bond manifests itself by a prominent FT-IR band, raising its intensity through the dipole coupling. Similarly, the hydrogen bonding manifests itself in the FT-IR spectrum with complex features covering the range of $\sim 1300\text{--}1150 \text{ cm}^{-1}$. The corresponding Raman bands reflect the stretching ring contributions with rather medium intensities. The infrared active vibrations are due to the mixed, in-plane and out-of-plane—or more precisely—spatially intermediate O—H \cdots N deformations of very large amplitude. Such large-amplitude proton displacement gives a strong charge fluctuation, due to the internal OH \cdots O interactions, resulting in prominent IR response. It is interesting to note that, according to the theory, the lowest band in the discussed range undergoes a spectacular damping of intensity upon inclusion of the dipole-coupling term. The nature of this vibration is interesting, as in fact the collective, *ungerade*-type proton displacement induces the possibly maximal polarization. The mode transforms the structure into the ferroelectric-like state. Nevertheless, since the crystal structure is centrosymmetric, with an opposite orientation of the neighboring chains, the crystal structure definitely corresponds to the paraelectric phase. It should be noted that the out-of-plane

deformation localized on each O—H \cdots N moiety does not contribute noticeably to the IR spectrum, as being predicted with a large separation at ~ 1250 and 970 cm^{-1} for the stronger and weaker H-bonds, respectively.

The remaining modes, giving noticeable Raman and infrared signals at 1026 and 973 cm^{-1} , respectively, can be generally assigned to the trigonal β DMP deformation and the antisymmetric, Kekule-type BrA stretching.

$925\text{--}125 \text{ cm}^{-1}$. The range beneath 925 cm^{-1} was further explored by combining optical and inelastic neutron scattering spectroscopy to emphasize the hydrogen dynamics. In Figure 7a, the experimental INS spectrum, recorded at 10 K, is presented against the results of the zone-center lattice dynamics calculations. All the tested methodologies provide no significant differences in the range above 300 cm^{-1} . Before switching to the low-wavenumber range, we will analyze the upper part of the spectrum in more detail.

The amplitude-weighted vibrational density of states (VDOS/ $G(\nu)$) spectra were calculated both at the Γ point as well as by including the phonon dispersion (BZ) with the representative PBE fixed-cell methodology. By analyzing Figure 7b, one can note nearly flat phonon dispersion branches in the upper part of the spectrum. The analyzed dispersion relations did not reveal any imaginary frequencies, which suggests that there is no mechanical instability expressing a phonon-driven displacive

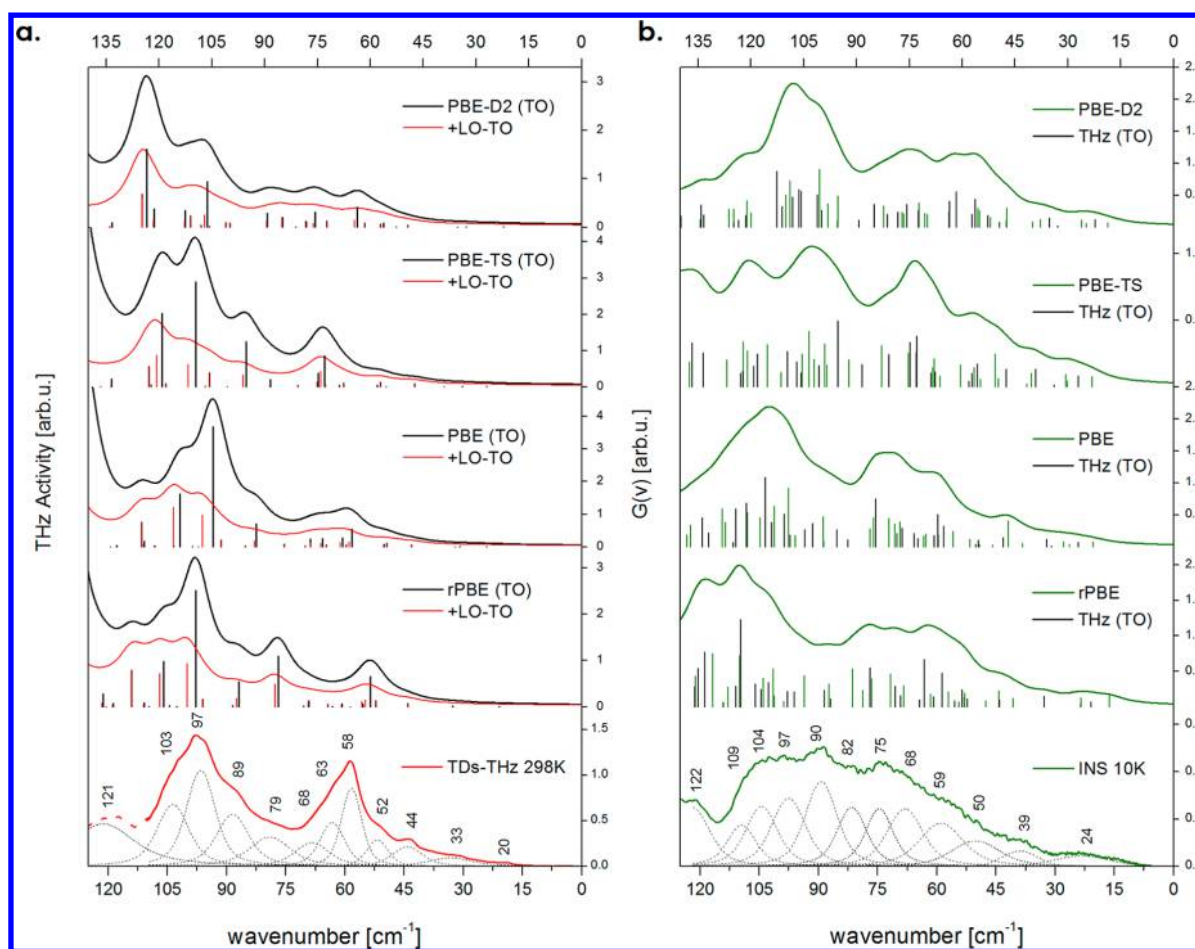


Figure 8. Theoretical and experimental low-wavenumber TDs-THz at 298 K (a) and INS at 10 K (b) spectra of BrA:2,6-DMP (1:1) co-crystal. The presented theoretical results were obtained from CASTEP plane-wave DFT calculations. The *ungerade* phonon contributions to the INS spectrum are denoted with black sticks. Note that the theoretical data are presented in the broadened scale of 140–0 cm^{-1} , in order to account for a slight systematic overestimation of the calculated low wavenumbers.

tendency and that no low-temperature transition would be expected.

The simulated Γ -point VDOS spectrum has been further presented against the dispersion-averaged spectrum as well as with the one obtained with inclusion of the LO–TO splitting (see Figure 7b). It is clearly shown that all of these effects are negligible in the present case. Furthermore, the one-phonon $0 \rightarrow 1$ harmonic spectrum at the Γ point has been presented against the total spectrum including higher-order transitions. It has been clearly shown that, except for the anharmonic features (ν') at ~ 700 – 600 and 450 cm^{-1} , the low-temperature INS spectrum can be perfectly described in the harmonic approach.

Figure 7b also refers to the partial VDOS contributions along the relative atomic displacement contribution in each phonon mode (see the histogram). As may be clearly seen, the INS spectrum is completely dominated by the hydrogen vibrations in 2,6-DMP. The upper part of the spectrum refers mainly to the C–H deformations, while the lower part is generally covered by CH_3 contributions. Although the BrA molecules contribute to the spectrum through the OH deformations, their bonding with base molecules obviously affects the DMP vibrational dynamics.

In contrast, the nearly perfectly simulated infrared and Raman spectra are mainly attributed to the ring deformations, which are assigned in detail in Table 6. A more detailed spectral analysis shows that the highest-wavenumber band around 870 cm^{-1} is a tail of large-amplitude CH wagging modes coupled to the CH_3

rocking vibrations. Beneath, one can see the trigonal BrA deformation contributing to spectra at $\sim 800 \text{ cm}^{-1}$. Since the ring deformation induces the in-plane $\nu(\text{O}–\text{H}\cdots\text{N})$ motion, it gives a prominent IR signal and a noticeable INS band. Similarly, the second contribution to the INS spectrum at $\sim 775 \text{ cm}^{-1}$ comes from the BrA twisting deformations coupled to the puckering modes of DMP, which affects the proton motion in a similar way. The puckering DMP deformations also induce the CH movement, which gives rise to the INS band at 741 cm^{-1} . The spectral gap of ~ 700 – 575 cm^{-1} is covered by overtone trails, contributing to the INS and IR spectra.

The bands found around 560 and 530 cm^{-1} in the INS spectra are due to asymmetric in-plane and out-of-plane DMP deformations which contribute to the VDOS spectra through the so-called riding effect of methyl groups. The similar CH_3 riding effect can be linked to the INS bands found at ~ 415 , 290 , and 230 cm^{-1} , respectively.

The prominent bands were also observed with IR and Raman at $\sim 515 \text{ cm}^{-1}$ due to the BrA quadratic deformation. The trigonal, asymmetric BrA deformation contributes to the INS spectrum at $\sim 500 \text{ cm}^{-1}$ through the OH riding effect by engaging large amplitude oxygen movement as can be seen in the amplitude histogram from Figure 7b. Similarly, the large amplitude of oxygen motion, due to the in-phase $\delta(\text{CCO})$ deformation (contributing to the RS signal), manifests itself as a double-band at $\sim 370 \text{ cm}^{-1}$ in the INS spectrum. Since such

Table 7. Collection of Experimentally Identified FT-IR, FT-RS, and INS Wavenumbers (ν , cm^{-1}) for the BrA:2,6-DMP (1:1) Complex in the Low-Wavenumber Range along with a Tentative Band Assignment^a

S.	Theory - PBE - Γ		Experiment			Tentative Mode Assignment
	LO	TO	THz	RS	INS	
	ν [cm ⁻¹]		ν [cm ⁻¹]			
A _u	125.0	125.0	121			$\gamma\text{BrA}^{(\gamma\text{C}=\text{O}-\gamma\text{C}-\text{O})}$; $\tau(\text{C}_{(12)}\text{H}_3)^{\text{DMP}}$; DMP lib. $\angle bc$
B _u	124.4	124.1			122	$\tau(\text{C}_{(11)}\text{H}_3)^{\text{DMP}}$; $\gamma\text{BrA}^{(\gamma\text{C}=\text{O}-\gamma\text{C}-\text{O})}$; DMP lib. $\angle ab$
B _g		120.9		114		$\tau(\text{C}_{(11)}\text{H}_3)^{\text{DMP}}$; $\gamma\text{BrA}^{(\gamma\text{C}=\text{O}-\gamma\text{C}-\text{O})}$; DMP lib. $\angle bc$
A _u	115.8	115.8			109	$\tau(\text{C}_{(11)}\text{H}_3)^{\text{DMP}}$; $\gamma\text{BrA}^{(\gamma\text{C}=\text{O}-\gamma\text{C}-\text{O})}$; DMP lib. $\angle ac$
B _u	115.8	114.0	103		104	$\tau(\text{C}_{(11)}\text{H}_3)^{\text{DMP}}$; $\gamma\text{BrA}^{(\gamma\text{C}=\text{O}-\gamma\text{C}-\text{O})}$; DMP lib. $\angle ab$
B _g		113.3		102		$\tau(\text{C}_{(11)}\text{H}_3)^{\text{DMP}}$; $\gamma\text{BrA}^{(\gamma\text{C}=\text{O}-\gamma\text{C}-\text{O})}$; DMP lib. $\angle ab$
A _g		109.3			97	$\tau(\text{C}_{(11)}\text{H}_3)^{\text{DMP}}$; $\gamma\text{BrA}^{(\text{oop} \rightarrow \text{Br C6O4H2} \leftarrow)}$; DMP lib. $\angle ac$
B _U	107.7	104.7	97			$\nu\text{N}\cdots\text{O}$ ($\tau\text{BrA } \angle ab$; transl. DMP $\rightarrow a$); $\tau(\text{C}_{(12)}\text{H}_3)^{\text{DMP}}$
B _G		99.4			90	$\gamma\text{BrA}^{(\text{oop} \rightarrow \text{Br C6O4H2} \leftarrow)}$; DMP lib. $\angle ab$; $\tau(\text{C}_{(12)}\text{H}_3)^{\text{DMP}}$
A _g		95.5		93		$\nu\text{N}\cdots\text{O}$ (transl. DMP $\rightarrow a + \gamma\text{BrA}^{(\text{oop} \rightarrow \text{Br C6O4H2} \leftarrow)}$; $\tau(\text{C}_{(12)}\text{H}_3)^{\text{DMP}}$
B _u	92.9	92.4	89			$\nu\text{N}\cdots\text{O}$ ($\gamma\text{BrA}^{(\text{oop} \rightarrow \text{Br C6O4H2} \leftarrow)}$ + transl. DMP $\rightarrow b$)
A _g		85.1		82	82	DMP lib. $\angle ac$; $\tau(\text{C}_{(12)}\text{H}_3)^{\text{DMP}}$
B _u	84.5	84.5	79			DMP lib. $\angle bc$; $\gamma\text{BrA}^{(\text{oop} \rightarrow \text{Br C6O4H2} \leftarrow)}$; $\tau(\text{C}_{(12)}\text{H}_3)^{\text{DMP}}$
B _g		80.7			75	DMP lib. $\angle bc$; $\gamma\text{BrA}^{(\text{oop} \rightarrow \text{Br C6O4H2} \leftarrow)}$; $\tau(\text{C}_{(12)}\text{H}_3)^{\text{DMP}}$
B _g		77.6		72		DMP lib. $\angle ab$; BrA lib. $\angle ac$
B _u	74.1	73.6	68		68	DMP lib. $\angle ab$; BrA lib. $\angle ac$
B _u	68.5	67.9	63			$\gamma\text{BrA}\cdots\text{DMP } \angle ab (+ - - +)$; $\gamma\text{BrA}^{(\text{oop} \rightarrow \text{Br C6O4H2} \leftarrow)}$
A _U	66.9	66.9			59	$\gamma\text{BrA}\cdots\text{DMP } \angle ab (+ + + +)$
B _U	66.0	65.3	58			$\delta\text{BrA}\cdots\text{DMP } \angle ab (+ - - +)$; $\gamma\text{BrA}^{(\text{oop} \rightarrow \text{Br C6O4H2} \leftarrow)}$
A _g		57.7			50	$\gamma\text{BrA}\cdots\text{DMP } \angle ab (+ - - +)$; $\gamma\text{BrA}^{(\text{oop} \rightarrow \text{Br C6O4H2} \leftarrow)}$
B _u	56.3	56.1	52			Breathing mode $\rightarrow b (\uparrow \downarrow \downarrow \uparrow)$; $\gamma\text{BrA}^{(\text{oop} \rightarrow \text{Br C6O4H2} \leftarrow)}$
A _u	48.3	48.3	44			Screwing $\tau\text{DMP } \angle ab (+ + + +)$
A _g		46.8			39	Screwing $\tau\text{DMP } \angle ab (+ - + -)$
A _u	36.0	36.0			24	Shearing BrA $\rightarrow a (+ - - +)$
B _u	34.6	34.6	33			Screwing $\tau\text{BrA } \angle bc (+ - + -)$
A _g		31.1				Chain Shearing BrA $\rightarrow a (+ + - -)$
B _g		29.5				Chain Shearing BrA $\rightarrow c (+ - + -)$
A _u	27.1	27.1	20			Chain Shearing BrA $\rightarrow c (+ - - +)$
A _g		22.8				Chain Shearing $\rightarrow c (+ + - -)$

^aThe experimental data are presented against the results of the zone-center lattice dynamics calculations (fixed-cell PBE/1050 eV data). The symmetry (S) is noted for each transverse optical (TO) mode. The theoretical wavenumbers for the *ungerade* modes are given for both transverse and longitudinal components. See the Supporting Information for an extended version of the table.

vibration leads to the internal $\nu(\text{H}\cdots\text{O})$ fluctuations, it is also well-resolved in the FT-IR spectrum. The similar out-of-phase $\delta(\text{CCO})$ deformation results in a barely visible shoulder band observed in the INS spectrum at 305 cm^{-1} .

The skeletal deformations contribute to the optical spectra at lower wavenumbers, while the INS spectrum reveals its most intense components below 250 cm^{-1} , which are attributed to methyl torsional vibrations $\tau(\text{CH}_3)$. While such modes practically do not affect dipole moment nor polarizability, INS is a unique technique allowing to observe such vibrations. First of all, it should be noted that the background, isolated molecule calculations, performed at the PBE/6-31++G(d,p) level, predict the $\tau(\text{CH}_3)$ modes as the energetically lowest ones, with the wavenumbers of 66 and 74 cm^{-1} . The subsequent calculations for the isolated BrA:2,3-DMP model shift the wavenumbers up to 112 and 121 cm^{-1} . However, the solid-state influence is much greater. The above-discussed crystal packing gives rise to the nonequivalency of both CH_3 fragments. Such an effect was suggested in the Intermolecular Interactions section and very slightly reflected in the NMR spectrum. Such a subtle difference has a great influence on the INS spectrum. The $\text{C}(12)\text{H}_3$ groups are under stronger influence of the environment as being closer to the heavy atoms as well as to the pyrazine surface. It has already been clearly shown in Figure 4b, indicating prominent $\pi\cdots\text{CH}_3$ interactions. Most of the calculations predict the large-amplitude—very localized— $\tau\text{C}(12)\text{H}_3$ modes at 226 cm^{-1} , with a negligible IR and RS activity. Such a value is significantly

overestimated, as the quoted vibrations give a clear contribution to the INS spectrum, with the most intense band at 189 cm^{-1} . The discrepancy can be linked to an overestimation of the CH_3 rotational barrier by the tested methodology.

The second prominent band was found in the INS spectrum at 211 cm^{-1} . The theory predicts the related vibrations to be spread in the range of $\sim 210\text{--}190\text{ cm}^{-1}$. The background, isolated molecule calculations predict the two lowest deformation modes of DMP at 200 and 174 cm^{-1} , while the same calculations predict three deformation modes of BrA at 223 , 192 , and 162 cm^{-1} . All of these modes contribute to the INS through the riding effect, also giving well resolved bands in the optical spectra around 210 cm^{-1} . Since there are no more DMP deformation modes, one can observe a small gap down to $\sim 150\text{ cm}^{-1}$, which, however, cannot be attributed to the separation between internal and lattice vibrations.

As can be found in Figure 7b, the system reveals a large density of vibrational states beneath 150 cm^{-1} , which corresponds to $168\text{ } \Gamma$ -point vibrations, making a full assignment problematic. As seen in the figure, the dispersion of the modes is, however, rather very small. The modes around $150\text{--}140\text{ cm}^{-1}$ correspond to the low-energy out-of-plane BrA deformations along with the DMP librations, approximately, in the $\angle bc$ plane. The vibrations contribute to the INS spectrum mainly through the riding effect. The remaining DMP internal vibrations due to $\tau(\text{C}(11)\text{H}_3)$ give some contribution to the modes around 140 cm^{-1} .

Terahertz Range ($<125\text{ cm}^{-1}$). In order to give more insight into the lowest-wavenumber range, the time-domain terahertz spectroscopy has been applied, which, in contrast to INS, allows here only the polar Γ -point phonons to be observed, being not contaminated by methyl torsions. In addition, the *gerade* modes were identified with the help of Raman spectroscopy down to the notch-filter cut, where, however, the intensities are modulated as going toward the elastic wing.

The recorded TDs-THz and INS spectra are presented in Figure 8 against the results obtained with the tested methodologies. The band shape was approximated by the set of Voigt functions. The collection of the identified vibrations has been given in Table 7 along with a tentative mode assignment.

By analyzing Figure 8a, one should note that each methodology predicts a strong intensity dumping upon inclusion of the long-range coupling. Hence, in the present case, we can limit our considerations to the TO species. It is interesting to note that inclusion of the semiempirical dispersion corrections does not necessary deliver any advantage over the standard fixed-cell PBE calculations. In line with our previous findings,⁶⁵ one can observe a visible upward shift of the terahertz wavenumbers. Such an effect has been minimized here by presenting the theoretical spectra in a slightly enlarged scale up to 140 cm^{-1} .

The computations suggest that the $\tau(\text{C}(11)\text{H}_3)$ vibrations dominate the upper part of the low-wavenumber INS spectrum. Thereby, the quoted modes can be mainly attributed to the INS spectrum around 110 cm^{-1} , where there is no strong response in the THz spectrum. The reason why the $\text{C}(11)\text{H}_3$ has much lower wavenumbers can be attributed to their larger separation from the electron-donating moieties. The quoted vibrations are clearly coupled to the DMP librations and the low-energy out-of-plane BrA deformations $\gamma\text{BrA}(\gamma\text{C}=\text{O}\uparrow - \gamma\text{C}=\text{O}\downarrow)$. Thus, their wavenumbers are widespread down to $\sim 80\text{ cm}^{-1}$.

An intense absorption band found in the TDs-THz spectrum at 97 cm^{-1} can be described as the H-bond bridge $\nu\text{N}\cdots\text{O}$ stretching, giving the related maxima at 97 and 89 cm^{-1} , respectively. Since the INS response involves the $\text{C}(11)\text{H}_3$ torsion, the related mode does not clearly contribute to the VDOS spectrum.

According to the theory, both molecules undergo librations in the range of $\sim 80\text{--}70\text{ cm}^{-1}$, while the lowest internal vibration of BrA, associated with a contrary bromine–quinone out-of-plane translation, contributes down to $\sim 60\text{ cm}^{-1}$.

The nature of the remaining modes is very characteristic. Due to a large mass difference of both molecules, one can further observe the modes which can be approximated as the out-of-plane γ ($\text{BrA}\cdots\text{DMP}$) and in-plane δ ($\text{BrA}\cdots\text{DMP}$) bridge deformations and directly found in the TDs-THz spectrum. The former one gives a shoulder band at 63 cm^{-1} , while the latter contributes as the peak at 58 cm^{-1} .

Finally, due to the long-range hydrogen bonding and stacking interactions, very specific collective vibrations occur. At higher wavenumbers, one can expect the purely translational, “breathing” mode of the whole stacked chains, toward the *b*-axis. Its *ungerade* combination with the out-of-phase ($\uparrow\downarrow\uparrow$) translations of the neighboring layers contributes to the TDs-THz spectrum at 52 cm^{-1} . Beneath, one can observe the screwing, helical modes of the hydrogen-bonded DMP molecules, giving weak TDs-THz and INS bands around 40 cm^{-1} . Finally, the shearing modes occur, corresponding to the collective, parallel translations of the stacked layers. The modes manifest themselves as the extremely lowest band at 20 cm^{-1} in the TDs-THz spectrum. The quoted vibrations also clearly

contribute as a broad INS band, where the dispersed acoustic modes also contribute.

The vibrational analysis over the entire wavenumber range leads to several conclusions. In summary, one may note that, despite the quasi-harmonic approximation, the lattice dynamics calculations in the frame of semilocal DFT provide the results of excellent accuracy, allowing for possibly full understanding of the spectral features in both optical and neutron spectroscopy.

The presence of highly ordered, hydrogen-bonded polymer chains leads to several peculiarities in the vibrational spectrum. First of all, the nonequivalency of the hydrogen bonds leads to a significant chains polarization. Such a property is reflected in anomalously large Born charge tensor components and consequently results in prominent LO–TO splitting. The polarization effects significantly affect the infrared spectrum, which is completely dominated by the longitudinal components. The polarization effects are however negligible here for the wavenumber range below 1000 cm^{-1} . While the higher-wavenumber range is a structural marker in the research of polar molecular crystals and the infrared spectroscopy is the method of choice, the role of the LO–TO splitting should not be underrated.

The inelastic neutron spectroscopy along with the lattice-dynamics calculations clearly show that there is very limited dispersion of the phonon branches and there are no soft modes which would indicate a possible mechanic instability. The polymeric configuration is hence very stable with a one-dimensional conjugation defined by the hydrogen bonding. The layered structure of the hypothetical, infinite crystal is here further stabilized by the stacking interactions between the aromatic moieties. Such a configuration leads to highly localized vibrations even in the terahertz range. As a result, one can observe very characteristic collective vibrations of the molecular layers.

One should note that, according to the presented calculations, the long-awaited implementation of the dispersion-corrected density functional perturbation theory does not outperform the standard, fixed-cell lattice-dynamics calculations.

IV. CONCLUSIONS

The complementary structural and vibrational spectroscopy study of bromanilic acid:2,6-dimethylpyrazine (BrA:2,6-DMP) 1:1 co-crystal is presented by combining single-crystal X-ray diffraction with computationally supported solid-state spectroscopy.

The structural analysis revealed that the title system crystallized in the monoclinic $P2_1/c$ space group, with four molecular units per conventional cell. The crystal structure can be described as an infinite net of antiparallely oriented hydrogen bonded molecular chains.

The crystallographic analysis was supported by intermolecular analysis, which revealed nonequivalency of the moderate-strength hydrogen-bonding interactions and the presence of multiple specific intermolecular forces. The nature of the weak interactions has been characterized with the help of Hirshfeld surface and reduced density gradient approaches, which have underlined the role of stacking interactions and weak van der Waals forces in crystal structure stabilization. The structural properties were linked to the solid-state NMR and vibrational spectroscopy, providing the identification of most characteristic features. The extended vibrational analysis was performed over the entire spectral range by confronting the optical spectroscopy in the middle, far, and terahertz range with neutron scattering.

The spectral analysis of the crystal phase was fully supported by the *state-of-the-art* periodic density functional theory calculations. The solid-state DFT methodology was thoroughly examined as referring to the structural properties and vibrational response. The performance of the recently implemented dispersion-corrected linear response methodology was extensively tested over the entire spectral range. With an example of a large molecular system, significantly affected by intermolecular interactions, we were able to show that the quoted approach does not necessarily lead to a remarkable improvement if referring to the well-adjusted fixed-cell GGA computations.

Nevertheless, despite quasi-harmonic approximation, an excellent agreement between the theoretical and experimental spectra has been achieved, allowing for possibly complete interpretation of characteristic features and understanding of multiple peculiarities. Particularly, the lattice-dynamics calculations revealed the role of a significant long-range dipole coupling on the infrared response of the system along with the influence of the structure on the low-wavenumber vibrations.

■ ASSOCIATED CONTENT

■ Supporting Information

Figure showing the superposition of the X-ray and theoretical crystal structures of the title compound. Tables showing the set of internal coordinates found experimentally and theoretically, the diagonal components of the calculated Born-effective-charge tensor for noncarbon ions, the full collection of FT-IR, FT-RS, and INS wavenumbers complex along with a tentative band assignment in the medium- and low-wavenumber range. The Supporting Information is available free of charge on the ACS Publications website at DOI: 10.1021/acs.jpcb.5b03279.

■ AUTHOR INFORMATION

Corresponding Author

*E-mail: k.luczynska@ichtj.waw.pl.

Notes

The authors declare no competing financial interest.

■ ACKNOWLEDGMENTS

This research was supported in part by PL-Grid Infrastructure (Grant IDs: phd2013, phd2014). K.Ł. and K.D. gratefully acknowledge the financial support of Polish Government Plenipotentiary for JINR in Dubna (Grant Nos.: 118-8/1069-5/2014, 44/27-01-2015/7/1121/5). We would like to express our appreciation to Dr Norbert Palka (Military University of Technology, Warsaw); Dr Jerzy Antonowicz (Warsaw University of Technology); Ms. Zofia Huppenthal (Nicolaus Copernicus University, Torun); Ms. Halina Thiel-Pawlicka (Adam Mickiewicz University, Poznan); and Prof. Edward Mikuli (Jagiellonian University, Cracow) for the access to the research equipment and experimental support. We are also grateful to Prof. Denis P. Kozlenko (JINR, Dubna) for supporting the research mobility of K.Ł. and K.D. The FT-FIR spectrum was recorded thanks to the financial support of the European Regional Development Fund in the framework of the Polish Innovation Economy Operational Program (Contract No. POIG.02.01.00-12-023/08).

■ DEDICATION

This work is dedicated to the memory of Professor Janusz Leciejewicz (1928–2014).

■ REFERENCES

- (1) Zaman, B.; Tomura, M.; Yamashita, Y. Crystal Engineering Using Anilic Acids and Dipyrindyl Compounds through a New Supramolecular Synthon. *J. Org. Chem.* **2001**, *66*, 5987–5995.
- (2) Adam, M. S.; Parkin, A.; Thomas, L. H.; Wilson, C. C. Bifurcated Hydrogen-Bonded Synthons in Molecular Complexes of Picolines With Chloranilic Acid. *CrystEngComm* **2010**, *12*, 917–924.
- (3) Thomas, L. H.; Adam, M. S.; O'Neill, A.; Wilson, C. C. Utilizing Proton Transfer to Produce Molecular Salts in Bromanilic Acid Substituted-Pyridine Molecular Complexes - Predictable Synthons? *Acta Crystallogr., Sect. C* **2013**, *69*, 1279–1288.
- (4) Murata, T.; Morita, Y.; Yakiyama, Y.; Fukui, K.; Yamochi, H.; Saito, G.; Nakasui, K. Hydrogen-Bond Interaction in Organic Conductors: Redox Activation, Molecular Recognition, Structural Regulation, and Proton Transfer in Donor-Acceptor Charge-Transfer Complexes of TTF-Imidazole. *J. Am. Chem. Soc.* **2007**, *129*, 10837–10846.
- (5) Dengl, A.; Beyer, R.; Peterseim, T.; Ivek, T.; Untereiner, G.; Dressel, M. Evolution of Ferroelectricity in Tetrathiafulvalene-p-Chloranil as a Function of Pressure and Temperature. *J. Chem. Phys.* **2014**, *140*, 244511–244516.
- (6) Horiuchi, S.; Ishii, F.; Kumai, R.; Okimoto, Y.; Tachibana, H.; Nagaosa, N.; Tokura, Y. Ferroelectricity Near Room Temperature in Co-Crystals of Nonpolar Organic Molecules. *Nat. Mater.* **2005**, *4*, 163–166.
- (7) Horiuchi, S.; Kumai, R.; Tokura, Y. Room-Temperature Ferroelectricity and Gigantic Dielectric Susceptibility on a Supramolecular Architecture of Phenazine and Deuterated Chloranilic Acid. *J. Am. Chem. Soc.* **2005**, *127*, 5010–5011.
- (8) Horiuchi, S.; Kumai, R.; Tokura, Y. Hydrogen-Bonded Donor-Acceptor Compounds for Organic Ferroelectric Materials. *Chem. Commun.* **2007**, *23*, 2321–2329.
- (9) Bonnard, G.; Barrès, A. L.; Danten, Y.; Allis, D. G.; Mentré, O.; Tomerini, D.; Gatti, C.; Izgorodina, E. I.; Poizotab, P.; Frayret, C. Experimental and Theoretical Studies of Tetramethoxy-p-benzoquinone: Infrared Spectra, Structural and Lithium Insertion Properties. *RSC Adv.* **2013**, *3*, 19081–19096.
- (10) Tomura, M.; Yamashita, Y. One-Dimensional Supramolecular Tapes in the Co-Crystals of 2,5-Dibromo-3,6-Dihydroxy-1,4-Benzoquinone (Bromanilic Acid) with Heterocyclic Compounds Containing a Pyrazine Ring Unit. *CrystEngComm* **2000**, *2*, 92–95.
- (11) Seaton, C. C.; Blagden, N.; Munshi, T.; Scowen, I. J. Creation of Ternary Multicomponent Crystals by Exploitation of Charge-Transfer Interactions. *Chem.—Eur. J.* **2013**, *19*, 10663–10671.
- (12) Ip, B. C. K.; Shenderovich, I. G.; Tolstoy, P. M.; Frydel, J.; Denisov, G. S.; Buntkowsky, G.; Limbach, H. H. NMR Studies of Solid Pentachlorophenol-4-Methylpyridine Complexes Exhibiting Strong OHN Hydrogen Bonds: Geometric H/D Isotope Effects and Hydrogen Bond Coupling Cause Isotopic Polymorphism. *J. Phys. Chem. A* **2012**, *116*, 11370–11387.
- (13) Sheldrick, G. M. A Short History of SHELX. *Acta Crystallogr.* **2008**, *A64*, 112–122.
- (14) Momma, K.; Izumi, F. VESTA 3 for Three-Dimensional Visualization of Crystal, Volumetric and Morphology Data. *J. Appl. Crystallogr.* **2011**, *44*, 1272–1276.
- (15) Natkaniec, I.; Chudoba, D.; Hetmańczyk, Ł.; Kazimirov, V. Yu.; Krawczyk, J. I.; Sashin, L.; Zalewski, S. Parameters of the NERA Spectrometer for Cold and Thermal Modulators of the IBR-2 Pulsed Reactor. *J. Phys.: Conf. Ser.* **2014**, *554*, 012002.
- (16) Clark, S. J.; Segall, M. D.; Pickard, C. J.; Hasnip, P. J.; Probert, M. J.; Refson, K.; Payne, M. C. First Principles Methods Using CASTEP. *Z. Kristallogr.* **2005**, *220*, 567–570.
- (17) Refson, K.; Clark, S. J.; Tulip, P. R. Variational Density-Functional Perturbation Theory for Dielectrics and Lattice Dynamics. *Phys. Rev. B* **2006**, *73*, 155114–155136.
- (18) Perdew, J. P.; Burke, K.; Wang, Y. Generalized Gradient Approximation for the Exchange-Correlation Hole of a Many-Electron System. *Phys. Rev. B* **1996**, *54*, 16533–16539.
- (19) Perdew, J. P.; Burke, K.; Ernzerhof, M. Generalized Gradient Approximation Made Simple. *Phys. Rev. Lett.* **1996**, *77*, 3865–3868.

- (20) Haas, P.; Tran, F.; Blaha, P.; Schwarz, K. Construction of an Optimal GGA Functional for Molecules and Solids. *Phys. Rev. B* **2011**, *83*, 205117–205123.
- (21) Hammer, B.; Hansen, L. B.; Nørskov, J. K. Improved Adsorption Energetics Within Density-Functional Theory Using Revised Perdew-Burke-Ernzerhof Functionals. *Phys. Rev. B* **1999**, *59*, 7413–7421.
- (22) Perdew, J. P.; Chevary, J. A.; Vosko, S. H.; Jackson, K. A.; Pederson, M. R.; Singh, D. J.; Fiolhais, C. Atoms, Molecules, Solids, and Surfaces: Applications of the Generalized Gradient Approximation for Exchange and Correlation. *Phys. Rev. B* **1992**, *46*, 6671–6687.
- (23) Perdew, J. P.; Chevary, J. A.; Vosko, S. H.; Jackson, K. A.; Pederson, M. R.; Singh, D. J. Fiolhais, Erratum: Atoms, Molecules, Solids, and Surfaces: Applications of the Generalized Gradient Approximation for Exchange and Correlation. *Phys. Rev. B* **1993**, *48*, 4978–4978.
- (24) Wu, Z.; Cohen, R. E. More Accurate Generalized Gradient Approximation for Solids. *Phys. Rev. B* **2006**, *73*, 235116–235122.
- (25) Perdew, J. P.; Ruzsinszky, A.; Csonka, G. I.; Vydrov, O. A.; Scuseria, G. E.; Constantin, L. A.; Zhou, X.; Burke, K. Restoring the Density-Gradient Expansion for Exchange in Solids and Surfaces. *Phys. Rev. Lett.* **2008**, *100*, 136406–136410.
- (26) Grimme, S. Semiempirical GGA-Type Density Functional Constructed With a Long-Range Dispersion Correction. *J. Comput. Chem.* **2006**, *27*, 1787–1799.
- (27) Tkatchenko, A.; Scheffler, M. Accurate Molecular Van Der Waals Interactions from Ground-State Electron Density and Free-Atom Reference Data. *Phys. Rev. Lett.* **2009**, *102*, 073005–073009.
- (28) Rappe, A. M.; Rabe, K. M.; Kaxiras, E.; Joannopoulos, J. D. Optimized Pseudopotentials. *Phys. Rev. B* **1990**, *41*, 1227–1230.
- (29) Rappe, A. M.; Rabe, K. M.; Kaxiras, E.; Joannopoulos, J. D. Optimized Pseudopotentials – Erratum. *Phys. Rev. B* **1991**, *44*, 13175–13175.
- (30) Baroni, S.; Giannozzi, P.; Testa, A. Green's-Function Approach to Linear Response in Solids. *Phys. Rev. Lett.* **1987**, *58*, 1861–1864.
- (31) Gonze, X.; Allan, D. C.; Teter, M. P. Dielectric Tensor, Effective Charges, and Phonons in Neutron-Diffraction Studies of Salicylic Acid and α -Quartz by Variational Density-Functional Perturbation Theory. *Phys. Rev. Lett.* **1994**, *68*, 3603–3606.
- (32) Gonze, X. Perturbation Expansion of Variational Principles at Arbitrary Order. *Phys. Rev. A* **1995**, *52*, 1086–1095.
- (33) Gonze, X. Adiabatic Density-Functional Perturbation Theory. *Phys. Rev. A* **1995**, *52*, 1096–1114.
- (34) Gonze, X. Dynamical Matrices, Born Effective Charges, Dielectric Permittivity Tensors, and Interatomic Force Constants From Density-Functional Perturbation Theory. *Phys. Rev. B* **1997**, *55*, 10337–10354.
- (35) Baroni, S.; Dal Corso, A.; de Gironcoli, S.; Giannozzi, P. Phonons and Related Crystal Properties from Density-Functional Perturbation Theory. *Rev. Mod. Phys.* **2001**, *73*, 515–561.
- (36) Milman, V.; Perlov, A.; Refson, K.; Clark, S. J.; Gavartin, J.; Winkler, B. Structural, Electronic and Vibrational Properties of Tetragonal Zirconia Under Pressure: a Density Functional Theory Study. *J. Phys.: Condens. Matter* **2009**, *21*, 485404–485416.
- (37) Polavarapu, P. L. Ab initio Vibrational Raman and Raman Optical Activity Spectra. *J. Phys. Chem.* **1990**, *94*, 8106–8112.
- (38) Gonze, X.; Charlier, J. C.; Teter, M. P. Interatomic Force Constants from First Principles: The Case of α -Quartz. *Phys. Rev. B* **1994**, *50*, 13035–13038.
- (39) Ramirez-Cuesta, A. J. The New Version of the Software for Analyzing and Interpreting INS Spectra. *Comput. Phys. Commun.* **2004**, *157*, 226–238.
- (40) Pickard, C. J.; Mauri, F. All-Electron Magnetic Response With Pseudopotentials: NMR Chemical Shifts. *Phys. Rev. B* **2001**, *63*, 245101–245113.
- (41) Yates, J. R.; Pickard, C. J.; Mauri, F. Calculation of NMR Chemical Shifts for Extended Systems Using Ultrasoft Pseudopotentials. *Phys. Rev. B* **2007**, *76*, 024401–024412.
- (42) Asaji, T.; Amino, D.; Tago, N.; Mizuno, M. Proton Dynamics in One-Dimensional Hydrogen-Bonding System in Molecular Co-Crystals TMP-D2Ca and DMP-H2Ca. *Hyperfine Interact.* **2010**, *197*, 269–274.
- (43) Zhao, Y.; Schultz, N. E.; Truhlar, D. G. Design of Density Functionals by Combining the Method of Constraint Satisfaction with Parametrization for Thermochemistry, Thermochemical Kinetics, and Noncovalent Interactions. *J. Chem. Theory Comput.* **2006**, *2*, 364–382.
- (44) Zhao, Y.; Truhlar, D. G. The M06 Suite of Density Functionals for Main Group Thermochemistry, Thermochemical Kinetics, Noncovalent Interactions, Excited States, and Transition Elements: Two New Functionals and Systematic Testing of Four M06-Class Functionals and 12 Other Functionals. *Theor. Chem. Acc.* **2008**, *120*, 215–241.
- (45) Modrzejewski, M.; Chalaśiński, G.; Szczeniński, M. M. Range-Separated Meta-GGA Functional Designed for Noncovalent Interactions. *J. Chem. Theory Comput.* **2014**, *10*, 4297–4306.
- (46) Dion, M.; Rydberg, H.; Schroder, E.; Langreth, D. C.; Lundqvist, B. I. Van der Waals Density Functional for General Geometries. *Phys. Rev. Lett.* **2004**, *92*, 246401–4.
- (47) Dion, M.; Rydberg, H.; Schroder, E.; Langreth, D. C.; Lundqvist, B. I. Erratum: Van der Waals Density Functional for General Geometries. *Phys. Rev. Lett.* **2005**, *95*, 109902.
- (48) Langreth, D. C.; Dion, M.; Rydberg, H.; Schroder, E.; Hyldgaard, P.; Lundqvist, B. I. Van der Waals Density Functional Theory with Applications. *Int. J. Quantum Chem.* **2005**, *101*, 599–610.
- (49) Thonhauser, T.; Cooper, V. R.; Li, S.; Puzder, A.; Hyldgaard, P.; Langreth, D. C. Van der Waals Density Functional: Self-Consistent Potential and the Nature of the Van der Waals Bond. *Phys. Rev. B* **2007**, *76*, 125112–11.
- (50) King, M. D.; Blanton, T. N.; Korter, T. M. Revealing the True Crystal Structure of L-Phenylalanine Using Solid-State Density Functional Theory. *Phys. Chem. Chem. Phys.* **2012**, *14*, 1113–1116.
- (51) Druzbicki, K.; Mikuli, E.; Palka, N.; Zalewski, S.; Ossowska-Chruściel, M. D. Polymorphism of Resorcinol Explored by Complementary Vibrational Spectroscopy (FT-RS, THz-TDS, INS) and First-Principles Solid-State Computations (Plane-Wave DFT). *J. Phys. Chem. B* **2015**, *119*, 1681–1695.
- (52) McKinnon, J. J.; Mitchell, A. S.; Spackman, M. A. Hirshfeld Surfaces: A New Tool for Visualising and Exploring Molecular Crystals. *Chem.—Eur. J.* **1998**, *4*, 2136–2141.
- (53) Spackman, M. A.; McKinnon, J. J. Fingerprinting Intermolecular Interactions in Molecular Crystals. *CrystEngComm* **2002**, *4*, 378–392.
- (54) McKinnon, J. J.; Spackman, M. A.; Mitchell, A. S. Novel Tools for Visualizing and Exploring Intermolecular Interactions in Molecular Crystals. *Acta Crystallogr., Sect. B* **2004**, *60*, 627–668.
- (55) McKinnon, J. J.; Jayatilaka, D.; Spackman, M. A. Towards Quantitative Analysis of Intermolecular Interactions with Hirshfeld Surfaces. *Chem. Commun.* **2007**, 3814–3816.
- (56) Spackman, M. A.; Jayatilaka, D. Hirshfeld Surface Analysis. *CrystEngComm* **2009**, *11*, 19–32.
- (57) Johnson, E. R.; Keinan, S.; Mori-Sánchez, P.; Contreras-García, J.; Cohen, A. J.; Yang, W. Revealing Non-Covalent Interactions. *J. Am. Chem. Soc.* **2010**, *132*, 6498–6506.
- (58) Wolff, S. K.; Grimwood, D. J.; McKinnon, J. J.; Turner, M. J.; Jayatilaka, D.; Spackman, M. A. *Crystal Explorer*, version 3.1; University of Western Australia: Crawley, 2012.
- (59) Steiner, T. The Hydrogen Bond in the Solid State. *Angew. Chem., Int. Ed.* **2002**, *41*, 48–76.
- (60) Contreras-García, J.; Johnson, E. R.; Keinan, S.; Chaudret, R.; Piquemal, J. P.; Beratan, D. N.; Yang, W. NCIPLOT: a Program for Plotting Non-Covalent Interaction Regions. *J. Appl. Crystallogr.* **2010**, *43*, 1250–1260.
- (61) Hanson, R. M. Jmol - A Paradigm Shift in Crystallographic Visualization. *J. Appl. Crystallogr.* **2010**, *43*, 1250–1260.
- (62) Xu, Z.; Yang, Z.; Liu, Y.; Lu, Y.; Chen, K.; Zhu, W. Halogen Bond: Its Role Beyond Drug-Target Binding Affinity for Drug Discovery and Development. *J. Chem. Inf. Model.* **2014**, *54*, 69–78.
- (63) Ukmar, T.; Kaucic, V.; Mali, G. Solid-State NMR Spectroscopy and First-Principles Calculations: a Powerful Combination of Tools for the Investigation of Polymorphism of Indomethacin. *Acta Chim. Slov.* **2011**, *58*, 425–433.

- (64) Terskikh, V. V.; Lang, S. J.; Gordon, P. G.; Enright, G. D.; Ripmeester, J. A. ¹³C CP MAS NMR of Halogenated (Cl, Br, I) Pharmaceuticals at Ultrahigh Magnetic Fields. *Magn. Reson. Chem.* **2009**, *47*, 398–406.
- (65) Łuczyńska, K.; Druźbicki, K.; Łyczko, K.; Starosta, W. Complementary Optical and Neutron Vibrational Spectroscopy Study of Bromanilic Acid: 2,3,5,6-Tetramethylpyrazine (1:1) Cocrystal. *Vib. Spectrosc.* **2014**, *75*, 26–38.
- (66) Durman, R.; Favre, P.; Jayasooriya, U. A.; Kettle, S. F. A. Longitudinal Optical-Transverse Optical (L.O.-T.O.) Splitting on Internal Modes in the Raman Spectra of Noncentric Crystals. *J. Crystallogr. Spectrosc. Res.* **1987**, *17*, 431–484.
- (67) Balan, E.; Saitta, A. M.; Mauri, F.; Calas, G. First-Principles Modeling of the Infrared Spectrum of Kaolinite. *Am. Mineral.* **2001**, *86*, 1321–1330.
- (68) Parker, S. F.; Haris, P. I. Inelastic Neutron Scattering Spectroscopy of Amino Acids. *Spectroscopy* **2008**, *22*, 297–307.
- (69) Stroppa, A.; Di Sante, D.; Horiuchi, S.; Tokura, Y.; Vanderbilt, D.; Picozzi, S. Polar Distortions in Hydrogen Bonded Organic Ferroelectrics. *Phys. Rev. B* **2011**, *84*, 014101–5.
- (70) Mukhopadhyay, S.; Gutmann, M. J.; Jura, M.; Jochym, D. B.; Jimenez-Ruiz, M.; Sturniolo, S.; Refson, K.; Fernandez-Alonso, F. Ferroelectric Behaviour in Solid Croconic Acid Using Neutron Scattering and First-Principles Density Functional Theory. *Chem. Phys.* **2013**, *427*, 95–100.
- (71) Szczęśniak, M. M.; Kurnig, I. J.; Scheiner, S. Vibrational Frequencies and Intensities of H-Bonded and Li-Bonded Complexes. H₃N··HCl and H₃N··LiCl. *J. Chem. Phys.* **1988**, *89*, 3131–3138.
- (72) Balan, E.; Lazzeri, M.; Delattre, S.; Méheut, M.; Refson, K.; Winkler, B. Anharmonicity of Inner-OH Stretching Modes in Hydrous Phyllosilicates: Assessment from First-Principles Frozen-Phonon Calculations. *Phys. Chem. Miner.* **2007**, *34*, 621–625.
- (73) Denisov, G. S.; Mavri, J.; Sobczyk, L. *Potential Energy Shape for the Proton Motion in Hydrogen Bonds Reflected in Infrared and NMR Spectra. in Hydrogen Bonding—New Insights*; Grabowski, S. J., Ed.; Springer: Dordrecht, 2006; pp 377–416.
- (74) Witkowski, A. Infrared Spectra of the Hydrogen Bonded Carboxylic Acids. *J. Chem. Phys.* **1967**, *47*, 3645–3648.
- (75) Marechal, Y.; Witkowski, A. Infrared Spectra of H-Bonded Systems. *J. Chem. Phys.* **1968**, *48*, 3697–3705.
- (76) Witkowski, A.; Wójcik, M. Infrared Spectra of Hydrogen Bond a General Theoretical Model. *Chem. Phys.* **1973**, *1*, 9–16.
- (77) Wójcik, M. J. Theory of the Infrared Spectra of the Hydrogen Bond in Molecular Crystals. *Int. J. Quantum Chem.* **1976**, *10*, 747–760.
- (78) Frisch, M. J.; et al. *Gaussian 09*, revision D.1; Gaussian, Inc.: Wallingford, CT, 2009.
- (79) Druźbicki, K.; Mielcarek, J.; Kiwilsza, A.; Toupet, L.; Collet, E.; Pajzderska, A.; Wąsicki, J. Computationally Assisted (Solid-State DFT) Structural (X-Ray) and Vibrational Spectroscopy (FT-IR, FT-RS, TDs-THz) Characterization of the Cardiovascular Drug – Lacidipine. submitted to. *Cryst. Growth. Des.* **2015**, DOI: 10.1021/acs.cgd.5b00251.